


Coercivity Determines Magnetic Particle Heating

Journal Article**Author(s):**

Starsich, Fabian H.L.; Eberhard, Christian; Boss, Andreas; [Hirt, Ann Marie](#) ; Pratsinis, Sotiris E.

Publication date:

2018-10-10

Permanent link:

<https://doi.org/10.3929/ethz-b-000282025>

Rights / license:

[In Copyright - Non-Commercial Use Permitted](#)

Originally published in:

Advanced Healthcare Materials 7(19), <https://doi.org/10.1002/adhm.201800287>

Funding acknowledgement:

163243 - Multifunctional nanoparticles for targeted theranostics (SNF)

1
2 **Coercivity determines magnetic particle heating**

3
4
5 *Fabian H.L. Starsich¹, Christian Eberhardt², Andreas Boss², Ann. M. Hirt³, Sotiris E. Pratsinis^{1,*}*

6
7 ¹Particle Technology Laboratory, Institute of Process Engineering, Department of Mechanical and Process Engineering,

8 ETH Zurich, Sonneggstrasse 3, CH-8092 Zurich, Switzerland

9
10 ²Institute of Diagnostic and Interventional Radiology, University Hospital Zürich, Rämistrasse 100, CH-8091 Zürich,

11 Switzerland.

12
13 ³Institute of Geophysics, ETH Zürich, Sonneggstrasse 5, CH-8092 Zürich, Switzerland.

14
15 *Corresponding author:

16 Sotiris E. Pratsinis; Tel.: +41 44 632 31 80; fax: +41 44 632 15 95; e-mail: sotiris.pratsinis@ptl.mavt.ethz.ch

17
18
19 06.01.2021

20 Submitted to:

21 Advanced Healthcare Materials

22
23
24 ***"This is the peer reviewed version of the following article: Starsich, F. H. L., Eberhardt, C.,***
25 ***Boss, A., Hirt, A. M., Pratsinis, S. E., Adv. Healthcare Mater. 2018, 7, 1800287, which has been***
26 ***published in final form at <https://doi.org/10.1002/adhm.201800287>. This article may be used for***
27 ***non-commercial purposes in accordance with Wiley Terms and Conditions for Use of Self-***
28 ***Archived Versions."***

1 **Abstract:**

2 Diseased cell treatment by heating with magnetic nanoparticles is hindered by their required high
3 concentrations. A clear relationship between heating efficiency and magnetic properties of nanoparticles has
4 not been attained experimentally yet due to limited availability of magnetic nanoparticles with varying size
5 and composition. Here we use versatile flame aerosol technology for synthesis of 21 types of ferro-
6 /ferrimagnetic nanocrystals with varying composition, size and morphology for hyperthermia and
7 thermoablation therapy. Heating efficiency, magnetic hysteresis and first order reversal curves of these
8 materials are compared. The maximum heating performance occurs near the transition from
9 superparamagnetic to single domain state, regardless of particle composition. Most importantly, the ratio
10 between saturation magnetization and coercivity can be linked to the heating properties of magnetic
11 nanoparticles. Magnetic interaction is controlled by changes in the architecture of the nanoparticles and
12 closely analyzed by first order reversal curves. Silica-coated non-stoichiometric Gd-Zn ferrite exhibits the
13 most promising therapeutic capability at relatively low particle concentrations, as shown *in vitro* with
14 cancerous prostate cells.

15 **Keywords:** *magnetic particle heating, hyperthermia, coercivity, iron oxide*

16

17

18

19

20

21

22

23

24

25

1 **Introduction**

2 Magnetic nanoparticle heating refers to the temperature increase in ferro-/ferrimagnetic nanostructures
3 (typically iron oxides) and their surrounding medium (e.g. cancer cells) by an oscillating external magnetic
4 field.^[1] The inherent therapeutic applications are promising as biocompatible nanostructures can be locally
5 activated during treatment to thermally destroy diseased tissue and remain otherwise inactive. Therefore, the
6 therapeutic effect can be externally triggered and precisely controlled. This characteristic makes magnetic
7 nanoparticle heating superior over conventional chemotherapy where the injected drugs not only attack
8 cancerous sites but also healthy organs leading to severe side-effects.^[2] This advantage has attracted strong
9 interest and led to successful treatments of several malignant tissues, such as prostate cancer^[3] and
10 glioblastoma^[4]. Recent progress in the field with respect to material optimization and in vitro/in vivo studies
11 has been summarized extensively.^[5,6]

12 Despite these promising results, wide-spread clinical application is hindered, predominantly, by the required
13 large doses of magnetic nanostructures currently clinically used (112 mg mL⁻¹, 0.1-0.7 mL per mL tumor)^[7]
14 for effective thermal damage at the diseased site. This tremendous concentration of un-physiological material
15 might also bear some to date unknown risks of adverse effects and hence should be drastically lowered. For
16 example, nanoparticles were still detectable in the prostate even 17.5 months after administration.^[8]
17 Additionally, the required strong magnetic fields for a sufficient temperature increase leads to undesired
18 heating outside the target region.^[9] Reduced particle concentrations might also allow also allow monitoring
19 via magnetic resonance imaging.^[6] Furthermore, especially diffuse carcinomas are not suitable for direct
20 nanoparticle injection and therefore pose problems in a clinical routine. Under such circumstances, the
21 magnetic particles would have to be administered intravenously to target the diseased site via blood flow
22 which restricts their applied amounts even more (e.g. ~0.7 % of injected nanoparticles reach a cancerous
23 site).^[10] A deeper understanding of the relationship between particle characteristics (composition, size,
24 morphology) and their magnetically-driven heating of diseased cells would allow optimization of
25 nanostructured magnetic systems with respect to their heating efficiency for minimization of the required
26 nanoparticle dose.

27 Three mechanisms lead to the temperature increase of ferro-/ferrimagnetic nanostructures in an oscillating
28 magnetic field (Neel- and Brownian-relaxation, and hysteresis).^[11] For nanoparticles smaller than the

1 superparamagnetic limit (e.g. ~ 25 nm for Fe_3O_4), heat dissipates by either magnetic dipoles (Neel-relaxation)
2 or entire nanostructures (Brownian-relaxation) seeking to align with the oscillating magnetic field. Larger
3 nanoparticles (> 80 nm for Fe_3O_4) can be multi-domain systems, in which hysteresis effects in the form of
4 shifting domain walls dictate the thermal effects.^[11] Intermediately sized systems ($\sim 25 - 80$ nm for Fe_3O_4)
5 heat through a combination of all three effects while a clear separation is not possible. It is frequently
6 assumed that hysteresis heating is negligible for biomedical applications as comparably strong applied
7 magnetic fields^[12] and therefore large single domain magnetic particles are required.^[13] The underlying
8 dominant heating mechanism, however, strongly depends generally on the strength and frequency of the
9 applied magnetic field.^[14] Besides particle size, material composition^[15] or agglomeration^[16], and therefore
10 the applied synthesis method, also strongly influence heating efficiency. For example, iron oxides^[17], metal
11 iron^[18], iron cobalt^[19], cobalt ferrite^[20], manganese ferrite^[21], mesoporous silica nanoparticles^[22] or even
12 bacterial magnetosomes^[23] and magnetically complex core/shell systems^[24] have been reported as excellent
13 candidates for efficient magnetic particle heating.

14 The preceding simplified summary shows that theoretical predictions of magnetic particle heating effects are
15 a challenging task. An in-depth understanding of the interplay between mechanisms and effects dictating
16 magnetic particle heating is hindered by a missing wide-range experimental verification of the predominant
17 theoretical concepts. This might be due to limited ranges of nanoparticle sizes, compositions or
18 morphologies available by a single synthesis method.

19 Specific loss power (SLP) is frequently used^[11] to compare the magnetic heating efficiencies of nanoparticles
20 from different studies. However, it was recently shown, that the assumptions of linear dependence on
21 concentration and applied field amplitude are not valid.^[25] Furthermore, the initial temperature increase used
22 for calculating SLPs is not clearly defined. This makes a comparison of nanomaterials prepared by different
23 methods not straightforward, as surface properties, size-distribution or morphology can vary distinctively
24 between them.

25 Flame-spray synthesis might overcome that dilemma as it stands out for its product versatility.^[26] For
26 example, 18 different flame-made nanomaterials were compared with respect to their fluorescence
27 efficiency.^[27] Additionally, this dry process (no solvent-residues due to high-temperature combustion) is
28 scalable (> 1 kg h^{-1}),^[28] both representing key requirements for a successful product translation into clinical

1 application,^[29] being frequently overlooked. Moreover, with this technology several magnetic nanoparticles
2 of various sizes and compositions, such as Co,^[30] FeC,^[31] Fe_xO_y,^[32] or SiO₂-coated Fe₂O₃^[33] and
3 Zn_{0.4}Fe_{2.6}O₄^[34] have been prepared.

4 Basic magnetic properties of such ferro-/ferrimagnetic nanoparticles can be analyzed with hysteresis curves
5 providing their saturation magnetization (M_s) and coercivity (B_c). The B_c in particular strongly depends on
6 the size of the ferro-/ferrimagnetic system.^[35] It remains close to zero for small superparamagnetic (SP)
7 structures and then increases suddenly in the simple single-domain (SD) regime. The B_c is therefore an
8 excellent parameter to evaluate the SP-SD transition size for various material compositions and
9 morphologies. More detailed information about the magnetic properties of nanomaterials can be obtained
10 from first order reversal curve (FORC) measurements.^[36] They provide information on the B_c distribution,
11 revealing deeper insight into morphology as well as crystal structure^[37], instead of (merely) averaged
12 coercivity as given by hysteresis curves,

13 This study aims to systematically elucidate, for the first time to our knowledge, the correlation of magnetic
14 and material properties with magnetic particle heating efficiencies experimentally, for a wide-range of
15 material compositions and sizes in defined experimental conditions. To this end, 21 magnetic nanoparticles
16 of various sizes, compositions and morphologies were prepared by aerosol technology. Their magnetic
17 properties were closely analyzed and compared to their heating efficiency. For an in-depth understanding,
18 FORCs of representative systems were investigated providing information on the distribution of magnetic
19 properties. Capitalizing on this knowledge, the ferro-/ferrimagnetic nanoparticles were carefully engineered
20 to increase the magnetic particle heating effect. The most promising nanoparticle system, silica-coated
21 Gd_{0.225}Zn_{0.4}Fe_{2.375}O₄, was further evaluated with *in vitro* studies on human PC3 prostate cancer cells.

22

23 **Experimental**

24 *Particle synthesis*

25 Various ferro-/ferrimagnetic bare and SiO₂-coated iron oxide based nanoparticles (NP), containing Zn and/or
26 Gd were prepared by flame-spray pyrolysis (FSP).^[33] Table S1 summarizes the process conditions for their
27 synthesis. In brief, a liquid precursor solution was fed at 5-8 mL min⁻¹ through a capillary and was thereafter

1 dispersed with 3-5 L min⁻¹ O₂ (all gases PanGas AG, purity > 99%) into fine droplets. The pressure drop
2 over the capillary was constant at 1.6 bar. The resulting spray was ignited and stabilized by a premixed
3 CH₄/O₂ (1.5 / 3.2 L min⁻¹) support flame. The spray flame was enclosed by a quartz glass tube (ID = 45 mm)
4 of various lengths (Table S1) and sheathed with 40 L min⁻¹ O₂. The liquid precursors were prepared by
5 dissolving the required amounts of iron(III) nitrate nonahydrate (Sigma-Aldrich, purity 98%), zinc-nitrate
6 hexahydrate (Sigma-Aldrich, purity 98%) and gadolinium(III) nitrate hexahydrate (Sigma-Aldrich, purity
7 99.99%) in a 1:1 volume mixture of 2-ethylhexanoic acid (2-EHA, Sigma-Aldrich, 99%) and ethanol. Prior
8 to production all liquid precursors were magnetically stirred for at least 1 h at room temperature.

9 The SiO₂-coating was applied by swirl-injection of Hexamethyldisiloxane (HMDSO, Sigma-Aldrich, purity
10 ≥ 99%) vapor through a torus ring with 16 equally spaced openings, facing 20° upstream.^[33] The HMDSO
11 vapor was obtained by feeding N₂ through a bubbler filled with HMDSO placed in a water bath at 20°C and
12 thereafter diluting it with 15 L min⁻¹ of additional N₂. The nominal SiO₂ content in the product was varied by
13 adapting the N₂ flow through the bubbler, according to calculations at saturation conditions. Downstream the
14 HMDSO injection, the particle stream was enclosed also by another quartz glass tube (ID = 45 mm, length =
15 30 cm), which allowed extensive mixing of HMDSO vapor and FSP-made nanoparticles facilitating their
16 SiO₂-coating. All nanomaterials were collected further downstream on a glass-fiber filter (Whatman GF6,
17 257 mm diameter) with the aid of a vacuum pump (Busch, Seco SV 1040C). No further treatment of the
18 powder was conducted. The quartz tubes were pre-heated for 2 min by combusting particle-free solvent.

19 SiO₂-coated (35 wt%) Gd_{0.225}Zn_{0.4}Fe_{2.375}O₄ (7.5 at% Gd) nanoparticles were surface functionalized with
20 polyethylene glycol (PEG) via melt grafting, as described elsewhere in detail.^[38] In brief, 300 mg
21 nanoparticles were ground with 9 g Poly(ethylene glycol) monomethyl ether (MW 5000 g mol⁻¹, Sigma-
22 Aldrich) in a mortar and transferred to a double-neck round-bottom flask. Then they were flushed for 30 min
23 under argon atmosphere at room temperature. Thereafter, they were heated to 200 °C under argon
24 atmosphere for 4 h. After cooling down, the mixture was washed three times with each dichloromethane,
25 ethanol and water via sonication (Branson, 40 kHz) and centrifugation (7800 rpm). Finally the pellet was
26 dried in air.

27

1 *Characterization*

2 Crystal sizes were determined by X-ray diffraction (XRD, Bruker AXS D8 Advanced diffractometer, Cu K α ,
3 40 kV) and fitting of the main diffraction peak ($2\theta \approx 35.6^\circ$) via Topas 4 software and the Scherrer equation.

4 Lattice parameters were obtained by Rietveld analysis using ICSD 084611 and an internal NiO standard.^[39]

5 Diffraction patterns were aligned to that standard.

6 The specific surface area (SSA) was measured by a five-point isotherm and the Brunauer-Emmett-Teller
7 method (BET, Micromeritics Tristar II PLUS) at 77K. Prior to measurement, all samples were degassed for 1
8 h at 150 °C. Average primary particle diameters, d_{BET} , were calculated from the SSA, assuming a

9 composition-dependent density and spherical shape. Magnetic hysteresis curves and FORCs were obtained
10 by a vibrating sample magnetometer (VSM, Princeton Measurement Corporation), as described elsewhere.^[37]

11 Scanning transmission electron microscopy (TEM) images were acquired on a Hitachi HD-2700VD with
12 probe corrector (CEOS) at an acceleration potential of 200 kV (electron gun: cold-field emitter) in the ultra-
13 high resolution mode. Dynamic light scattering measurements were performed on a Zetasizer (Malvern
14 Instruments) right after sonication for 5 min (Branson, 40 kHz).

15 The performance of all nanoparticles (NP) for magnetic particle heating was evaluated with 2.5 mg of
16 magnetic material in 8 μL dimethyl sulfoxide (DMSO). Eppendorf tubes of these colloidal solutions were
17 subjected to an oscillating magnetic field (Magnetherm, NanoTherics Ltd., UK, frequency = 512 kHz,
18 intensity = 14.08 kA m^{-1}) and the temperature was measured by an infrared camera (Fluke, Ti110). Prior to
19 measurement, each dispersion was sonicated in a bath for 5 min (Branson, 40 kHz). Magnetic particle
20 heating efficiency was assessed in triplicates (mean \pm SD).

21 *In vitro studies*

22 In vitro biocompatibility was assessed with adherent prostate cancer cells (PC-3, ATCC® CRL-1435, USA)
23 and non-adherent monocytes (THP-1). The PC-3 cells were cultivated in supplemented growth medium
24 (Gibco™ RPMI 1640, Thermo Fisher Scientific) with 10% fetal bovine serum (Gibco™, Thermo Fisher
25 Scientific) and 1% penicillin/streptomycin (PenStrep, Gibco, Thermo Fisher Scientific) at 37 °C under
26 humidified atmosphere containing 5% CO₂. The PC3 cells were seeded at a density of 10 000 cells/well in a
27 flat bottom 96-well plate (100 μL per well) and cultured for 24 h.

1 For co-incubation of NP with PC-3 cells, sterile nanoparticle suspensions were prepared in unsupplemented
2 RPMI 1640 (Gibco™ RPMI 1640, Thermo Fisher Scientific) and autoclaved for 20 min at 121°C. Desired
3 NP concentrations were adjusted with unsupplemented RPMI 1640 and twofold supplemented growth
4 medium at least 45 min prior co-incubation with PC-3 cells. Growth medium in the flat bottom 96-well plate
5 was replaced with thoroughly vortexed NP suspensions securing sample homogeneity and subsequently
6 incubated for further 24 h. For the PC-3 cells, the 96-well plate containing them was centrifuged at 500g for
7 5 min at room temperature (RT). The supernatant (50 µL/ well) was transferred in a new flat bottom 96-well
8 plate. The released lactate dehydrogenase activity was determined applying 50 µL of CytoTox 96 reagent
9 according to manufacturer instructions (CytoTox 96 Non Radioactive Cytotoxicity Assay, Promega,
10 Madison, WI USA) and incubated in the dark at RT for 15 min. The absorbance was measured at 490 nm
11 using a plate reader (Epoch 2, BioTek Instruments, VT, USA).

12 THP-1 cells were cultivated, seeded and incubated with nanoparticles according to previous work.^[40] After
13 incubation, the contents of the wells was extracted and centrifuged at 6000g for 5 min. The supernatant (50
14 µL) was mixed in a new well with 50 µL of CytoTox 96 reagent and incubated in the dark at RT for 30 min.
15 Thereafter the absorption was measured at 490 nm by a plate reader (Mithras2 LB 943).

16 For *in vitro* magnetic particle heating, the PC-3 cells were seeded in non-pyrogenic cell culture dishes with a
17 diameter of 35 mm (35 mm x 10 mm, treated polystyrene, # 430165, Corning GmbH, Germany) at a density
18 of 200 000 cells/dish and cultured in 2 mL growth medium at 37 °C under humidified atmosphere containing
19 5% CO₂. Medium within the dishes was replaced with 1.5 mL fresh growth medium supplemented with the
20 nanoparticle suspensions at desired concentrations prior to nanoparticle hyperthermia experiments. Samples
21 were subjected to an oscillating magnetic field (Magnetherm, NanoTherics Ltd., UK, frequency = 512 kHz,
22 intensity = 18.77 kA m⁻¹) for 15 min. The contents of the dishes were extracted and afterwards centrifuged at
23 6000g for 5 min. The supernatant (50 µL) was used to determine the released lactate dehydrogenase activity
24 with 50 µL of CytoTox 96 reagent and incubated in the dark at RT for 30 min. The absorbance was
25 measured at 490 nm using a plate reader (Epoch 2, BioTek Instruments, VT, USA). *In vitro* studies were
26 performed in two separate experiments with quadruplicate measurements (total 8 values, mean ± SD).

27

1 Results and Discussion

2 Variation of composition and size

3 A series of 21 different magnetic $Gd_xZn_{0.4}Fe_{2.6-x}O_4$ NP with varying Gd content, size and SiO_2 -coating
 4 thickness were prepared by FSP^[34] and investigated as agents for magnetic particle heating. The amount of
 5 Zn was chosen to boost their magnetic properties^[41] compared to pure iron oxide. Table 1 summarizes their
 6 nominal compositions and measured size and properties, which are discussed in detail later on.

Table 1: Size and properties of as-prepared flame-made magnetic nanoparticles.

<i>Composition</i>			<i>Properties</i>					
Formula	Gd	SiO₂		d_{BET}	d_{XRD}	ΔT after 10 min	M_s	B_{CH}
	at%	wt%		nm	nm	°C	emu g ⁻¹	mT
Zn_{0.4}Fe_{2.6}O₄	0			35.3	35.1	0.83	73.42	9.48
Gd_{0.075}Zn_{0.4}Fe_{2.525}O₄	2.5			36.6	33.3	3.37	67.42	8.48
Gd_{0.15}Zn_{0.4}Fe_{2.45}O₄	5			33.6	25.5	6.97	53.06	5.99
Gd_{0.225}Zn_{0.4}Fe_{2.375}O₄	7.5			34.8	26.1	15.77	38.38	3.99
Gd_{0.3}Zn_{0.4}Fe_{2.3}O₄	10			36.4	23.4	19.1	25.72	1.99
Gd_{0.9}Zn_{0.4}Fe_{1.7}O₄	30			40.6	18.3	-0.17	1.37	1.48
Gd_{0.225}Zn_{0.4}Fe_{2.375}O₄	7.5			15.8	14.6	3.53	20.11	0.98
Gd_{0.225}Zn_{0.4}Fe_{2.375}O₄	7.5			21.9	22.5	29.87	35.24	0.98
Gd_{0.225}Zn_{0.4}Fe_{2.375}O₄	7.5			24.4	21.4	32	39.49	1.99
Gd_{0.225}Zn_{0.4}Fe_{2.375}O₄	7.5			28.5	22.6	24.1	35.85	2.49
Fe₂O₃	0			25	23	1.17	39.98	15.04
Zn_{0.4}Fe_{2.6}O₄	0			25.3	25.7	9.47	68.38	5.99
Gd_{0.225}Fe_{2.775}O₄	7.5			27	25.2	-0.67	3.88	6.49
Gd_{0.15}Zn_{0.4}Fe_{2.45}O₄	5			25.1	20.3	22.87	49.27	2.98
Gd_{0.3}Zn_{0.4}Fe_{2.3}O₄	10			27.8	21.1	25.97	28.09	0.98
Gd_{0.225}Zn_{0.4}Fe_{2.375}O₄	7.5			23.7	20.4	40.9	37.3	0.98
Gd_{0.225}Zn_{0.4}Fe_{2.375}O₄	7.5	5			23.8	13.7	45.99	2.49
Gd_{0.225}Zn_{0.4}Fe_{2.375}O₄	7.5	15			18.3	9.6	51.51	3.49
Gd_{0.225}Zn_{0.4}Fe_{2.375}O₄	7.5	25			14.3	23.5	50.64	2.98
Gd_{0.225}Zn_{0.4}Fe_{2.375}O₄	7.5	35			18.3	42.3	53.55	2.06
Gd_{0.225}Zn_{0.4}Fe_{2.375}O₄	7.5	50			17.5	34	44.85	2.06

7
 8 Figure 1 shows the XRD patterns of $Gd_xZn_{0.4}Fe_{2.6-x}O_4$ with varying Gd content and approximate $d_{BET} = 35$
 9 nm representative of all materials produced here (Figures S1-S4 show XRD patterns of remaining particles).
 10 The XRD pattern of pure $Zn_{0.4}Fe_{2.6}O_4$ is in excellent agreement to prior flame-made Zn-ferrites.^[34,42] Peaks
 11 corresponding to spinel ferrite (dashed line), which are identical^[43] to Fe_3O_4 , can clearly be observed for up

1 to 12.5 at% Gd. Note that the addition of Zn and/or Gd to the iron precursor prevents the formation of lesser
2 magnetic Fe₂O₃, which is typically obtained from oxygen-rich flames.^[32] For Gd contents above 5 at% there
3 is a peak at approximately 32° that could not be assigned to a common phase. Also the spinel-ferrite peak-
4 shift to lower angles due to a lattice expansion is in agreement with literature.^[41] This is verified by the inset
5 depicting the fitted lattice constant as a function of Gd content. The data follows a linear trend indicating the
6 successful incorporation of Gd atoms into the ZnFe matrix.^[44] Excessive Gd doping (30 at%) leads to the
7 predominant formation of a non-spinel structure (25-35°) that could not be assigned to a previously reported
8 phase.

9 **FIGURE 1**

10 Commonly, saturation magnetization, M_s , and coercivity, B_{CH} , which are easily determined from magnetic
11 hysteresis curves, are used to characterize the NP magnetic properties. Coercivity, however, has been largely
12 overlooked in connection with magnetic particle heating, but will be analyzed closely here. Also, the heating
13 efficiency is defined as the temperature increase from room-temperature ΔT of a particle dispersion after 10
14 min of exposure to an oscillating magnetic field.^[34]

15 Figure 2a shows the heating efficiency (left axis) and coercivity (right axis) of $Gd_xZn_{0.4}Fe_{2.6-x}O_4$ with $d_{BET} \approx$
16 25 (filled symbols) and 35 nm (open symbols) as a function of Gd content. The heating efficiency increases
17 similarly for both sizes due to Gd-addition into the ZnFe matrix until reaching a maximum at 7.5 at% Gd for
18 $d_{BET} \approx 25$ nm and 10 at% Gd for of $d_{BET} \approx 35$ nm. Increased Gd doping drastically reduces the performance.
19 This can be explained by the formation of a different crystal structure with strongly reduced M_s compared to
20 the non-stoichiometric ferrite phase formed at lower Gd contents (Figure 1a). The coercivity decreases with
21 increasing Gd content for both d_{BET} . Interestingly, for the investigated larger NP, although d_{BET} remains
22 constant at 35 nm, similar to coercivity, also the crystal size continuously decreases with increasing Gd
23 doping content, down to 27 nm (Figure S5). This suggests that crystal size rather than primary particle size
24 has a major influence on coercivity and thus on heating efficiency. At the same time, M_s decreases from 73
25 (0 at% Gd) down to 26 emu g⁻¹ (10 at% Gd), indicating that the benefit of low B_{CH} on magnetic heating is
26 stronger than that of high M_s . For the smaller particles ($d_{BET} \approx 25$ nm), both d_{BET} and d_{XRD} remain roughly
27 constant independent of Gd content, while B_{CH} , on the other hand, is decreasing. This suggests that by

1 addition of Gd the superparamagnetic limit shifts to larger sizes. Therefore, through the incorporation of Gd
2 together with Zn into the Fe-oxide matrix the magnetic properties could be optimized with respect to heating
3 efficiency through alterations in the spin structure.^[15,45]

4 **FIGURE 2**

5 The primary particle size of NP was tuned by varying precursor concentration and flame conditions (Table
6 S1). The TEM images (Figure S6) show that the morphology is not affected by primary particle size. The
7 primary particle size distribution is narrow (Figure S7) and good agreement between average primary
8 particle sizes determined from BET and TEM image counting is obtained. Figure 2b shows the heating
9 efficiency (left axis) and coercivity (right axis) for the most promising composition, $\text{Gd}_{0.225}\text{Zn}_{0.4}\text{Fe}_{2.375}\text{O}_4$
10 (corresponding to 7.5 at% Gd content), as a function of average primary particle diameter, d_{BET} . The heating
11 efficiency peaks at $d_{\text{BET}} = 23.7$ nm. A similar trend had been reported for flame-made $\text{Zn}_{0.4}\text{Fe}_{2.6}\text{O}_4$
12 (maximum at 21.4 nm)^[34] and other nanoparticles (maximum < 20 nm).^[46] Until the point of maximum
13 heating efficiency, coercivity remains low (at approximately 1 mT). This indicates that the NP are in the
14 superparamagnetic regime. For larger sizes, they shift into the single domain state with steadily increasing
15 coercivity and declining heating efficiency. This again emphasizes the necessity of low coercivity for
16 effective particle heating, which suggests that the maximum heating efficiency occurs at the transition size
17 from the superparamagnetic to the single-domain regime. Interestingly, the crystal size (Figure S8) commits
18 concomitantly a transition at the same coercivity limit, as it does not substantially increase for d_{BET} larger
19 than 23 nm. This might be due to formation of polycrystalline particles that increases coercivity and likewise
20 reduces heating efficiency.

21 *Variation of morphology through SiO₂-coating*

22 The most promising $\text{Gd}_{0.225}\text{Zn}_{0.4}\text{Fe}_{2.375}\text{O}_4$ (7.5 at% Gd and $d_{\text{BET}} \approx 24$ nm) NP with respect to heating
23 efficiency were *in situ* coated^[47] with SiO₂. This coating impacts the inter-particle distance between the
24 magnetic crystals within an aggregate.^[48] The TEM images (Figure 3) indicate rather uniform core/shell
25 morphology. The SiO₂ (bright fringe) evenly coats the core (dark area) and does not alter the particle
26 morphology, consistent with literature^[33]. Furthermore, increased SiO₂-content results in thicker and uniform
27 shells. The applied SiO₂-coating also promotes the surface functionalization of the magnetic nanoparticles.^[49]

FIGURE 3

1

2 Figure 4a shows their heating efficiency (left axis, per gram of active material) and coercivity (right axis) as
3 a function of their SiO₂ mass fraction (wt%). At low SiO₂ contents (5 wt% SiO₂), the heating efficiency is
4 reduced down to $\Delta T = 9.6$ °C. Thereafter it increases to $\Delta T = 42.3$ °C (35 wt% SiO₂), which resembles the
5 obtained ΔT values of bare particles ($\Delta T = 40.9$ °C). The heating efficiency is slightly reduced by further
6 addition of SiO₂ (50 wt%) that alters the magnetic particle-particle interactions. This trend is also indicated
7 by the coercivity which first increases at low SiO₂ contents and afterwards decreases again for higher ones.

FIGURE 4

8

9 The above described and commonly applied analysis of magnetic hysteresis curves, however, does not yield
10 direct information on magnetic interactions and only provides average bulk magnetic properties of
11 nanoparticles. First Order Reversal Curves (FORC), on the other hand, give closer insight into this magnetic
12 coupling and the effective magnetic size via the distribution of magnetic properties that strongly influence
13 the heating performance.

14 Therefore, the dependence of SiO₂-coating on magnetic interaction is analyzed in Figures 4b-d which show
15 FORCs of SiO₂-coated Gd_{0.225}Zn_{0.4}Fe_{2.375}O₄ (7.5 at% Gd, $d_{\text{BET}} \approx 24$ nm) with (a) 0, (b) 5 and (c) 35 wt% of
16 SiO₂ content. The horizontal B_{CF} (coercivity determined from FORC) spread around the FORC-maximum
17 describes the coercivity distribution. A broad vertical B_{UF} (interaction force) distribution around the
18 maximum can be related to a strong magnetic coupling.^[37] The FORC-maximum of a single domain
19 magnetic nanocrystal converges with decreasing size along the B_{CF} -axis towards the origin and marks the
20 superparamagnetic limit of approximately 20-25 nm (for Fe₃O₄)^[11]. For superparamagnetic crystals, the
21 FORC maximum continuously shifts upwards from the plot origin with decreasing crystal size.^[50]

22 The FORCs of bare (Figure 4b) and 35 wt% SiO₂-coated Gd_{0.225}Zn_{0.4}Fe_{2.375}O₄ (Figure 4d) are comparable.
23 Their maxima are shifted slightly up from the horizontal axis along the vertical axis indicating
24 superparamagnetism. Their distribution spread in all directions is tight suggesting a narrow size distribution.
25 A low SiO₂ content (Figure 4c, 5 wt%) leads to a similar location of the FORC maximum, however, also to a
26 broadening of the distribution (in both B_{CF} - and B_{UF} -direction) compared to the bare sample (Figure 4b). This

1 shows increased magnetic interactions by the close contact between magnetic particles. For higher SiO₂
2 contents (c, 35 wt%), however, the distributions narrows again similar to the bare sample as that contact is
3 reduced due to thicker silica film acting as a spacing material.^[48] This allows the magnetic nanoparticles to
4 act independently from each other. These changes in the magnetic particle-particle interactions also affect the
5 effective magnetic size, in line with Figure 2b. Reduced magnetic coupling leads to a reduced effective
6 magnetic size and therefore to a lower coercivity leading consequently to increased heating efficiency. This
7 suggests that solely by a change in particle aggregation, while keeping magnetic primary particle and crystal
8 sizes constant, the magnetic properties (i.e. coercivity) could be tuned.

9 The increased magnetic interaction for low SiO₂ contents compared to the bare sample is not intuitive and
10 requires further investigation. While earlier work on *in situ* SiO₂-coated Fe₂O₃ showed a continuous decrease
11 of the coercivity and a narrowing of the FORC distribution for increasing SiO₂ content,^[33,37] an increase in
12 coercivity similar to this work was recently observed for Zn_{0.4}Fe_{2.6}O₄^[34] and therefore potentially reflects a
13 dopant related effect. The observed changes in FORCs, however, confirm that magnetic interaction can be
14 controlled by carefully adjusting the SiO₂-coating thickness.

15 *Heating efficiency and magnetic properties*

16 Empirical determination of a measurable material property correlating to its magnetic particle heating
17 performance would be an attractive objective as it could provide quick and reliable means to select material
18 composition and characteristics. In practice, better efficiency would allow for lower particle dosages in
19 regard of a successful *in vivo* thermal therapy.

20 Figure 5a shows the heating efficiency of all prepared nanoparticles as a function of coercivity, B_{CH}, with
21 their associated saturation magnetization M_s (emu g⁻¹). The data follows a clear trend with low coercivities
22 having the highest heating efficiencies for all particles possessing ferro-/ferrimagnetic properties (M_s > 20
23 emu g⁻¹). This dependency can be described by the relationship $\Delta T = 40 / B_{CH}$ indicated with the dashed line.
24 Nevertheless, some particle compositions that had no coercivity were paramagnetic and have poor heating
25 efficiency. The variation in heating efficiency for nanoparticles with similar coercivity might be attributed to
26 their M_s (Figure 5a). Although a higher heating efficiency is loosely related to lower M_s, for comparable B_{CH},
27 a high M_s results in better heating efficiency. This is best illustrated by the linear dependency between M_s

1 normalized by B_{CH} and efficiency (Figure 5b), which is shown here for the first time to the best of our
2 knowledge. Most interestingly, this novel relationship between these material characteristics applies over
3 varying material compositions, morphologies as well as different size regimes which influence the various
4 heating mechanisms.^[51]

5 **FIGURE 5**

6 The frequently studied Rosensweig model^[52] does not report a direct dependence on coercivity, although
7 suggesting an increase in heating effect for high M_s . Dutz and Hergt et al.^[14,51,53,54] disputed the assumption
8 made in that model and indicate improved magnetic heating for large coercivities. Their experimental
9 verification, however, is restricted to heating effects inferred from hysteresis data. Here, it is shown that
10 maximum heating occurs for nanoparticles at the transition from superparamagnetic to single domain regime
11 (Figure 2b). This transition state, fulfills the condition that the applied field frequency equals the inverse of
12 the relaxation of the magnetic nanoparticles ($\omega\tau=1$).^[52] It should be noted that initial susceptibility, the ability
13 for a material to be magnetized, is also highest at the transition from superparamagnetic to single domain.
14 This transition boundary with respect to size depends on composition, as materials with similar particle sizes
15 and varying Gd contents (Figure 2a) show distinct differences in coercivity. Through the addition of Gd into
16 the ZnFe matrix (and also through the addition of Zn into the Fe matrix) the transition size can be altered,
17 allowing for larger M_s at the same B_{CH} and therefore increased heating efficiency. The transition size
18 theoretically depends on the applied field frequency.^[55] Here, coercivity was determined at 10 Hz whereas
19 heating measurements were conducted at 512 kHz. Despite this difference, both M_s/B_{CH} ratio and heating
20 efficiency follow the same trend. This suggests that the frequency dependency is only of minor concern,
21 especially in light of expected measurement uncertainties regarding heating efficiency and material
22 properties. This is in line with similar heating efficiency trends despite differences in applied frequencies.^[46]

23 *Biomedical application*

24 The $Gd_{0.225}Zn_{0.4}Fe_{2.375}O_4$ (7.5 at% Gd) with 35 wt% SiO_2 was the most promising composition here, due to
25 its highest heating efficiency. Note that the incorporation of Gd alone, omitting Zn doping, into the iron
26 oxide matrix ($Gd_{0.225}Fe_{2.775}O_4$) makes it inapplicable for any thermal treatment by eliminating all
27 superparamagnetic properties. At lower contents ($Gd_{0.02}Fe_{2.98}O_4$), however, Gd was shown to increase

1 heating efficiency.^[56] Here, only the presence of both Gd and Zn results in the strong increase in magnetic
2 heating efficiency due to reduced coercivity (Figures 2b, 4c). Sotiriou et al. ^[57] reported an ILP value of 0.74
3 nH m² kg⁻¹ for flame-made Fe₂O₃ of similar properties to those here (Figure 5a). The currently best
4 performing sample (SiO₂-coated Gd_{0.225}Zn_{0.4}Fe_{2.375}O₄) outperforms this material by a factor of 25. Therefore
5 it is a serious competition even to the best performing commercial and in literature reported systems, with
6 values between 0.15 and 3.1 nH m² kg⁻¹.^[58]

7 **FIGURE 6**

8 Finally, the biocompatibility of SiO₂-coated Gd_{0.225}Zn_{0.4}Fe_{2.375}O₄ for thermal therapy was analyzed *in vitro*.
9 To this end, the system was firstly investigated with respect to its cytotoxicity (Figure S9). Biocompatibility
10 up to 500 mg L⁻¹ with cancerous prostate PC3 cells and equally low cytotoxicity to leukemic THP1 cells as
11 commercially available SiO₂ (Aerosil 200, from MSDS: LD₅₀ > 3160 mg kg⁻¹) is shown. Thereafter, the
12 particles were added to PC3 cells at various concentrations and magnetically heated for 15 min, as well as
13 not heated as a control. Figure 6 shows the resulting cell death measured via Lactate dehydrogenase (LDH)
14 assay relative to full lysis. Cells with magnetic nanoparticles but no thermal treatment showed no toxicity.
15 For the lowest investigated concentration (8.3 mg mL⁻¹), no clear treatment effect could be observed. For
16 higher nanoparticle doses (> 16.7 mg mL⁻¹), however, a clear therapeutic effect of the magnetic heating can
17 be observed that increases for rising concentrations. Most importantly, the applied concentrations (< 33 mg
18 mL⁻¹) are all substantially lower than clinically used^[7] dispersions of 112 mg mL⁻¹. Furthermore, SiO₂-coated
19 (35 wt%) Gd_{0.225}Zn_{0.4}Fe_{2.375}O₄ (7.5 at% Gd) nanoparticles were surface-functionalized with polyethylene
20 glycol via scalable melt grafting.^[38] A stable hydrodynamic diameter of the PEGylated particles of
21 approximately 200 nm was measured for one hour, as shown in Figure S10.

22

23 **Conclusions**

24 The efficiency of 21 different flame-made ferro-/ferrimagnetic Gd-Zn-ferrite nanoparticles for magnetic
25 particle heating was compared. Particle morphology, size, composition and magnetic properties were
26 analyzed closely and contrasted to their heating efficiencies (ΔT after 10 min). This revealed that the best
27 performance of a ferro-/ferrimagnetic system is at its transition from superparamagnetic to single domain

1 state, at which the ratio of saturation magnetization to coercivity is maximized. As such it can serve as a
2 general criterion to optimize heating efficiency, independent of structural properties. This superparamagnetic
3 limit, however, is composition-dependent and could be adjusted by Zn-and Gd doping. Furthermore, by
4 SiO₂-coating, the magnetic coupling of the ferrite cores could be controlled precisely, as analyzed in detail by
5 first order reversal curves (FORCs). The Gd_{0.225}Zn_{0.4}Fe_{2.375}O₄ with 35 wt% SiO₂ coating was identified as the
6 most promising composition for magnetic particle thermal therapy at much lower concentration than
7 clinically applied amounts, as shown *in vitro* with cancerous prostate PC3 cells. However, more detailed
8 investigations under biological relevant conditions, such as inverted cell configurations^[59] or *in vivo* studies,
9 are required. The so far shown therapeutic efficiency and its dependence on particle coercivity along with the
10 employed scalable synthesis method and product biocompatibility renders the developed nanoparticles here
11 most promising for a fast translation to small-animal or even clinical studies.

12

13 **Acknowledgments:**

14 We thank Dr. Inge Herrmann (Empa, Switzerland) for assistance with the cytotoxicity studies. This research
15 was funded by the Swiss National Science Foundation (Grant: 205320_163243).

16

17 **References:**

- 18 [1] R. K. Gilchrist, R. Medal, W. D. Shorey, R. C. Hanselman, J. C. Parrott, C. B. Taylor, *Ann. Surg.*
19 **1957**, *146*, 596.
- 20 [2] C. L. Shapiro, A. Recht, *N. Engl. J. Med.* **2001**, *344*, 1997.
- 21 [3] M. Johannsen, U. Gneveckow, B. Thiesen, K. Taymoorian, C. H. Cho, N. Waldöfner, R. Scholz, A.
22 Jordan, S. A. Loening, P. Wust, *Eur. Urol.* **2007**, *52*, 1653.
- 23 [4] K. Maier-Hauff, F. Ulrich, D. Nestler, H. Niehoff, P. Wust, B. Thiesen, H. Orawa, V. Budach, A.
24 Jordan, *J. Neurooncol.* **2011**, *103*, 317.
- 25 [5] C. Blanco-Andujar, F. J. Teran, D. Ortega, *Iron Oxide Nanoparticles Biomed*, Elsevier, **2018**.

- 1 [6] K. Mahmoudi, A. Bouras, D. Bozec, R. Ivkov, C. Hadjipanayis, *Int. J. Hyperth.* **2018**.
- 2 [7] B. Thiesen, A. Jordan, *Int. J. Hyperth.* **2008**, *24*, 467.
- 3 [8] M. Johannsen, U. Gneveckow, K. Taymoorian, B. Thiesen, N. Waldöfner, R. Scholz, K. Jung, A.
4 Jordan, P. Wust, S. A. Loening, *Int. J. Hyperth.* **2007**, *23*, 315.
- 5 [9] M. Johannsen, B. Thiesen, P. Wust, A. Jordan, *Int. J. Hyperth.* **2010**, *26*, 790.
- 6 [10] S. Wilhelm, A. J. Tavares, Q. Dai, S. Ohta, J. Audet, H. F. Dvorak, W. C. W. Chan, *Nat. Rev. Mater.*
7 **2016**, *1*, 1.
- 8 [11] A. G. Kolhatkar, A. C. Jamison, D. Litvinov, R. C. Willson, T. R. Lee, *Int. J. Mol. Sci.* **2013**, *14*,
9 15977.
- 10 [12] H. Mamiya, *J. Nanomater.* **2013**, *2013*, 1.
- 11 [13] F. Gazeau, M. Lévy, C. Wilhelm, *Nanomedicine* **2008**, *3*, 831.
- 12 [14] R. Hergt, S. Dutz, M. Zeisberger, *Nanotechnology* **2010**, *21*, 15706.
- 13 [15] J. Jang, H. Nah, J.-H. Lee, S. Moon, M. Kim, J. Cheon, *Angew. Chemie Int. Ed.* **2009**, *48*, 1234.
- 14 [16] D. F. Coral, P. Mendoza Zélis, M. Marciello, M. D. P. Morales, A. Craievich, F. H. Sánchez, M. B.
15 Fernández van Raap, *Langmuir* **2016**, *32*, 1201.
- 16 [17] P. Guardia, R. Di Corato, L. Lartigue, C. Wilhelm, A. Espinosa, M. Garcia-Hernandez, F. Gazeau, L.
17 Manna, T. Pellegrino, *ACS Nano* **2012**, *6*, 3080.
- 18 [18] B. Mehdaoui, A. Meffre, L.-M. Lacroix, J. Carrey, S. Lachaize, M. Respaud, M. Gougeon, B.
19 Chaudret, *J. Appl. Phys.* **2010**, *107*, 09A324.
- 20 [19] J. Alonso, H. Khurshid, V. Sankar, Z. Nemat, M. H. Phan, E. Garayo, J. A. García, H. Srikanth, *J.*
21 *Appl. Phys.* **2015**, *117*, 17.
- 22 [20] A. Sathya, P. Guardia, R. Brescia, N. Silvestri, G. Pugliese, S. Nitti, L. Manna, T. Pellegrino, *Chem.*
23 *Mater.* **2016**, *28*, 1769.
- 24 [21] Y. Oh, N. Lee, H. W. Kang, Junghwan, *Nanotechnology* **2016**, *27*, 115101.

- 1 [22] C. Tao, Y. Zhu, *Dalt. Trans.* **2014**, *43*, 15482.
- 2 [23] E. Alphanbéry, S. Faure, O. Seksek, F. Guyot, I. Chebbi, *ACS Nano* **2011**, *5*, 6279.
- 3 [24] J. H. Lee, J. T. Jang, J. S. Choi, S. H. Moon, S. H. Noh, J. W. Kim, J. G. Kim, I. S. Kim, K. I. Park, J.
4 Cheon, *Nat. Nanotechnol.* **2011**, *6*, 418.
- 5 [25] I. Conde-Leboran, D. Baldomir, C. Martinez-Boubeta, O. Chubykalo-Fesenko, M. Del Puerto
6 Morales, G. Salas, D. Cabrera, J. Camarero, F. J. Teran, D. Serantes, *J. Phys. Chem. C* **2015**, *119*,
7 15698.
- 8 [26] R. Strobel, S. E. Pratsinis, *J. Mater. Chem.* **2007**, *17*, 4743.
- 9 [27] F. H. L. Starsich, P. Gschwend, A. Sergeyev, R. Grange, S. E. Pratsinis, *Chem. Mater.* **2017**, *29*,
10 8158.
- 11 [28] R. Mueller, L. Madler, S. E. Pratsinis, *Chem. Eng. Sci.* **2003**, *58*, 1969.
- 12 [29] N. Desai, *AAPS J.* **2012**, *14*, 282.
- 13 [30] R. N. Grass, W. J. Stark, *J. Mater. Chem.* **2006**, *16*, 1825.
- 14 [31] I. K. Herrmann, R. N. Grass, D. Mazunin, W. J. Stark, *Chem. Mater.* **2009**, *21*, 3275.
- 15 [32] R. Strobel, S. E. Pratsinis, *Adv. Powder Technol.* **2009**, *20*, 190.
- 16 [33] A. Teleki, M. Suter, P. R. Kidambi, O. Ergeneman, F. Krumeich, B. J. Nelson, S. E. Pratsinis, *Chem.*
17 *Mater.* **2009**, *21*, 2094.
- 18 [34] F. H. L. Starsich, G. A. Sotiriou, M. C. Wurnig, C. Eberhardt, A. M. Hirt, A. Boss, S. E. Pratsinis,
19 *Adv. Healthc. Mater.* **2016**, *5*, 2698.
- 20 [35] U. Jeong, X. Teng, Y. Wang, H. Yang, Y. Xia, in *Adv. Mater.*, **2007**, *19*, 33.
- 21 [36] M. Kumari, M. Widdrat, É. Tompa, R. Uebe, D. Schüler, M. Pósfai, D. Faivre, A. M. Hirt, *J. Appl.*
22 *Phys.* **2014**, *116*, 124304.
- 23 [37] A. M. Hirt, G. A. Sotiriou, P. R. Kidambi, A. Teleki, *J. Appl. Phys.* **2014**, *115*, 44314.
- 24 [38] K. Keevend, G. Panzarasa, F. H. L. Starsich, M. Zeltner, A. Spyrogianni, E. Tsolaki, G. Fortunato, S.

- 1 E. Pratsinis, S. Bertazzo, I. K. Herrmann, *Chem. Commun.* **2018**, 54, 2914.
- 2 [39] B. Ohtani, O. O. Prieto-Mahaney, D. Li, R. Abe, *J. Photochem. Photobiol. A Chem.* **2010**, 216, 179.
- 3 [40] M. T. Matter, F. Starsich, M. Galli, M. Hilber, A. A. Schlegel, S. Bertazzo, S. E. Pratsinis, I. K.
4 Herrmann, *Nanoscale* **2017**, 9, 8418.
- 5 [41] Y. Yang, X. L. Liu, Y. Yang, W. Xiao, Z. W. Li, D. S. Xue, F. S. Li, J. Ding, *J. Mater. Chem. C*
6 **2013**, 1, 2875.
- 7 [42] F. M. Hilty, A. Teleki, F. Krumeich, R. Buchel, R. F. Hurrell, S. E. Pratsinis, M. B. Zimmermann,
8 *Nanotechnology* **2009**, 20, 475101.
- 9 [43] S. H. Sun, H. Zeng, D. B. Robinson, S. Raoux, P. M. Rice, S. X. Wang, G. X. Li, *J. Am. Chem. Soc.*
10 **2004**, 126, 273.
- 11 [44] N. K. Prasad, K. Rathinasamy, D. Panda, D. Bahadur, *J. Mater. Chem.* **2007**, 17, 5042.
- 12 [45] J. H. Lee, Y. M. Huh, Y. Jun, J. Seo, J. Jang, H. T. Song, S. Kim, E. J. Cho, H. G. Yoon, J. S. Suh, et
13 al., *Nat. Med.* **2007**, 13, 95.
- 14 [46] A. E. Deatsch, B. A. Evans, *J. Magn. Magn. Mater.* **2014**, 354, 163.
- 15 [47] A. Teleki, M. C. Heine, F. Krumeich, M. K. Akhtar, S. E. Pratsinis, *Langmuir* **2008**, 24, 12553.
- 16 [48] G. A. Sotiriou, F. Starsich, A. Dasargyri, M. C. Wurnig, F. Krumeich, A. Boss, J. C. Leroux, S. E.
17 Pratsinis, *Adv. Funct. Mater.* **2014**, 24, 2818.
- 18 [49] F. Q. Tang, L. L. Li, D. Chen, *Adv. Mater.* **2012**, 24, 1504.
- 19 [50] C. R. Pike, A. P. Roberts, K. L. Verosub, *Geophys. J. Int.* **2001**, 145, 721.
- 20 [51] S. Dutz, R. Hergt, *Nanotechnology* **2014**, 25, 452001.
- 21 [52] R. E. Rosensweig, *J. Magn. Magn. Mater.* **2002**, 252, 370.
- 22 [53] S. Dutz, R. Hergt, J. Mürbe, R. Müller, M. Zeisberger, W. Andrä, J. Töpfer, M. E. Bellemann, *J.*
23 *Magn. Magn. Mater.* **2007**, 308, 305.
- 24 [54] R. Hergt, S. Dutz, M. Röder, *J. Phys. Condens. Matter* **2008**, 20, 385214.

- 1 [55] F. Hrouda, *Geophys. J. Int.* **2011**, *187*, 1259.
- 2 [56] P. Drake, H.-J. Cho, P.-S. Shih, C.-H. Kao, K.-F. Lee, C.-H. Kuo, X.-Z. Lin, Y.-J. Lin, *J. Mater.*
3 *Chem.* **2007**, *17*, 4914.
- 4 [57] G. A. Sotiriou, M. A. Visbal-Onufrak, A. Teleki, E. J. Juan, A. M. Hirt, S. E. Pratsinis, C. Rinaldi,
5 *Chem. Mater.* **2013**, *25*, 4603.
- 6 [58] M. Kallumadil, M. Tada, T. Nakagawa, M. Abe, P. Southern, Q. A. Pankhurst, *J. Magn. Magn.*
7 *Mater.* **2009**, *321*, 1509.
- 8 [59] A. Spyrogianni, I. K. Herrmann, M. S. Lucas, J. C. Leroux, G. A. Sotiriou, *Nanomedicine* **2016**, *11*,
9 2483.
- 10 [60] T. J. Brunner, P. Wick, P. Manser, P. Spohn, R. N. Grass, L. K. Limbach, A. Bruinink, W. J. Stark,
11 *Environ. Sci. Technol.* **2006**, *40*, 4374.

12

13

14

15

16

17

18

19

20

21

22

23

1 **Figure Captions:**

2 **Figure 1:** (a) X-ray diffraction patterns of $\text{Gd}_x\text{Zn}_{0.4}\text{Fe}_{2.6-x}\text{O}_4$ with varying Gd content (0-30 at%) and $d_{\text{BET}} =$
3 35 nm. Inset shows corresponding spinel-ferrite lattice constant as function of Gd content. Dashed line
4 indicates peaks for spinel ferrite, Fe_3O_4 .

5 **Figure 2:** Heating efficiency and coercivity (obtained from hysteresis curves) for (a) $\text{Gd}_x\text{Zn}_{0.4}\text{Fe}_{2.6-x}\text{O}_4$ with
6 d_{BET} of 25 (filled symbols) and 35 nm (open symbols) as a function of Gd content and for (b)
7 $\text{Gd}_{0.225}\text{Zn}_{0.4}\text{Fe}_{2.375}\text{O}_4$ (7.5 at% Gd) as a function of d_{BET} .

8 **Figure 3:** Transmission electron microscopy images of (a) bare $\text{Gd}_{0.225}\text{Zn}_{0.4}\text{Fe}_{2.375}\text{O}_4$ nanoparticles and
9 coated ones with (b) 15 and (c) 35 wt% SiO_2 .

10 **Figure 4:** (a) Heating efficiency and coercivity (obtained from hysteresis curves) for SiO_2 -coated
11 $\text{Gd}_{0.225}\text{Zn}_{0.4}\text{Fe}_{2.375}\text{O}_4$ (7.5 at% Gd, $d_{\text{BET}} = 24$ nm) as a function of SiO_2 content. Corresponding first order
12 reversal curves for samples with (a) 0, (b) 5 and (c) 35 wt% SiO_2 coating.

13 **Figure 5:** (a) Heating efficiency as a function of coercivity (obtained from hysteresis curves) for all 21
14 nanoparticle systems. Saturation magnetization M_s per gram of magnetic material is shown for each system.
15 (b) Heating efficiency as a function of the ratio of saturation magnetization to coercivity (obtained from
16 hysteresis curves, M_s/B_{CH}).

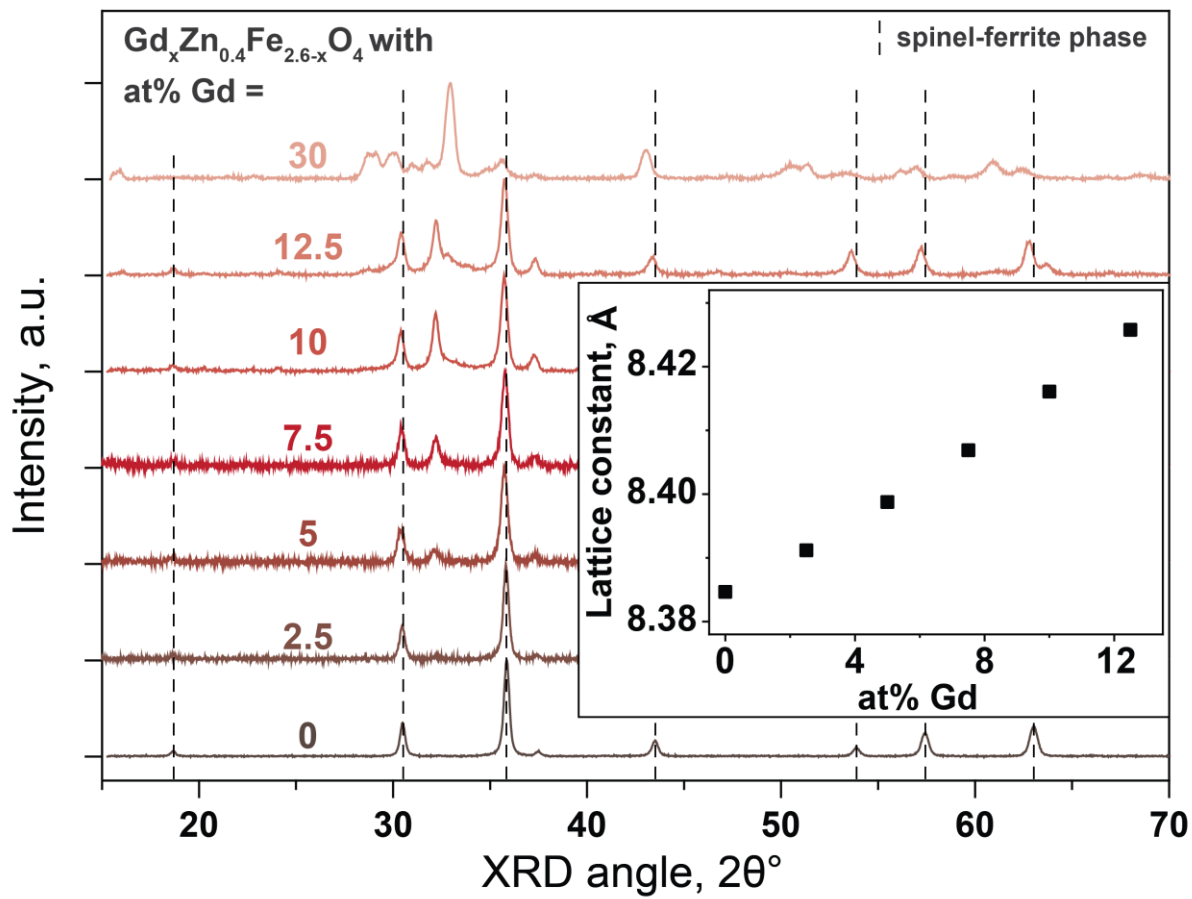
17 **Figure 6:** PC3 cell death relative full lysis (Triton X) under magnetic particle heating treatment of SiO_2
18 coated (35 wt%) $\text{Gd}_{0.225}\text{Zn}_{0.4}\text{Fe}_{2.375}\text{O}_4$ (7.5 at% Gd, $d_{\text{BET}} = 24$) at different particle concentrations.

19

20

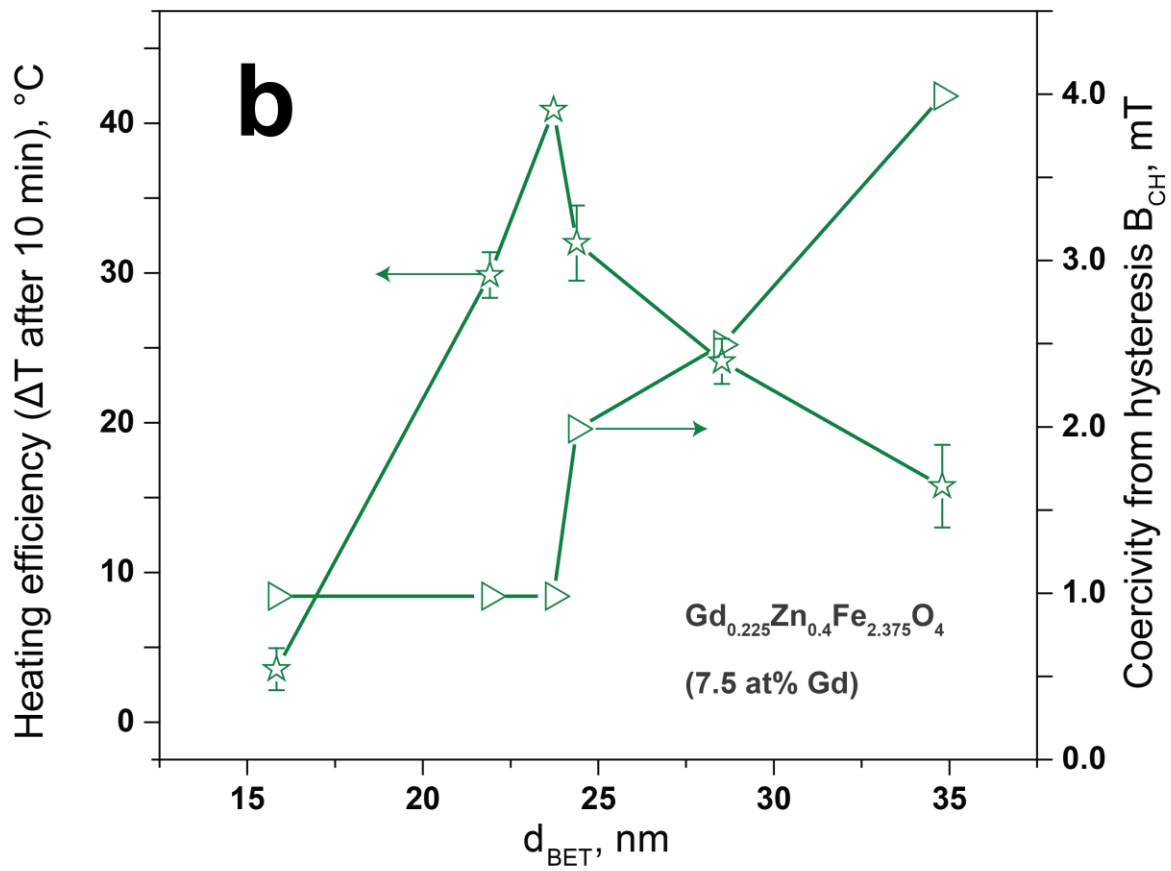
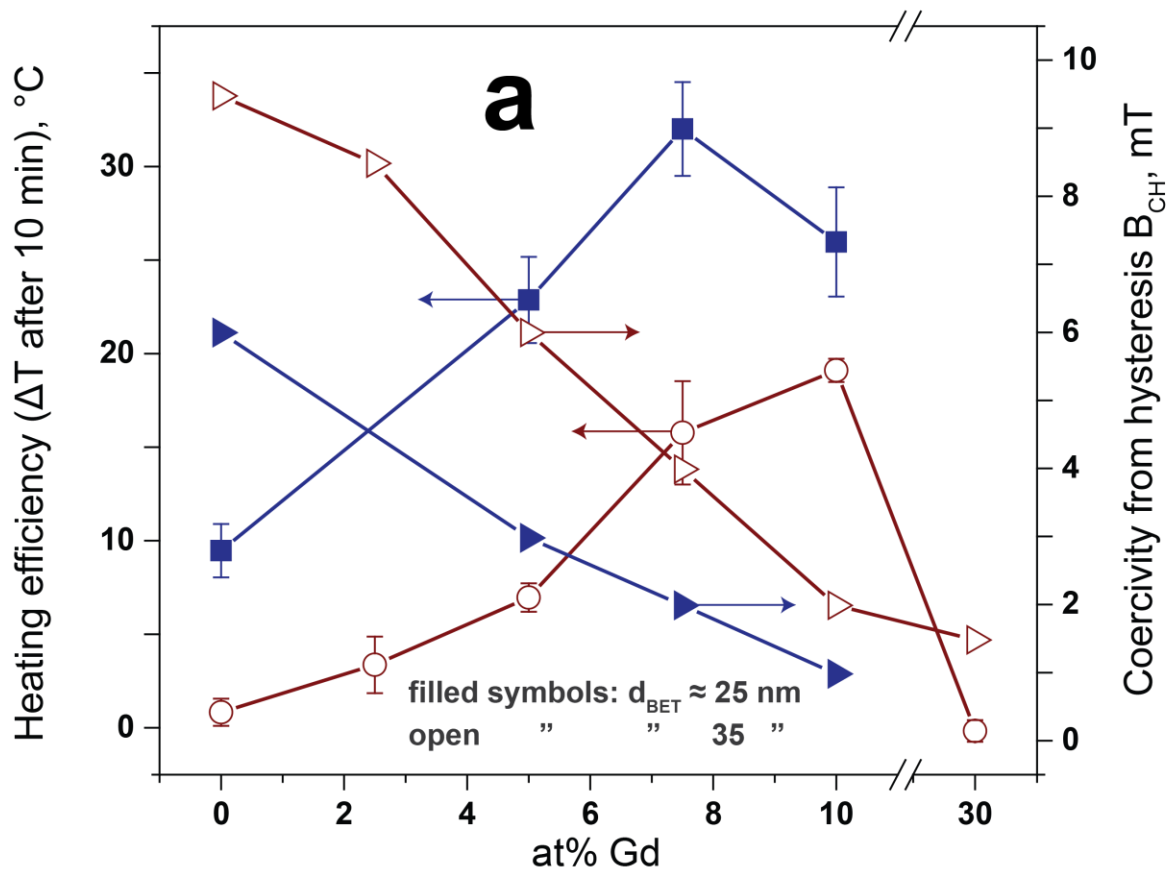
21

22 **Figures:**



1
2
3
4
5
6
7
8
9
10
11

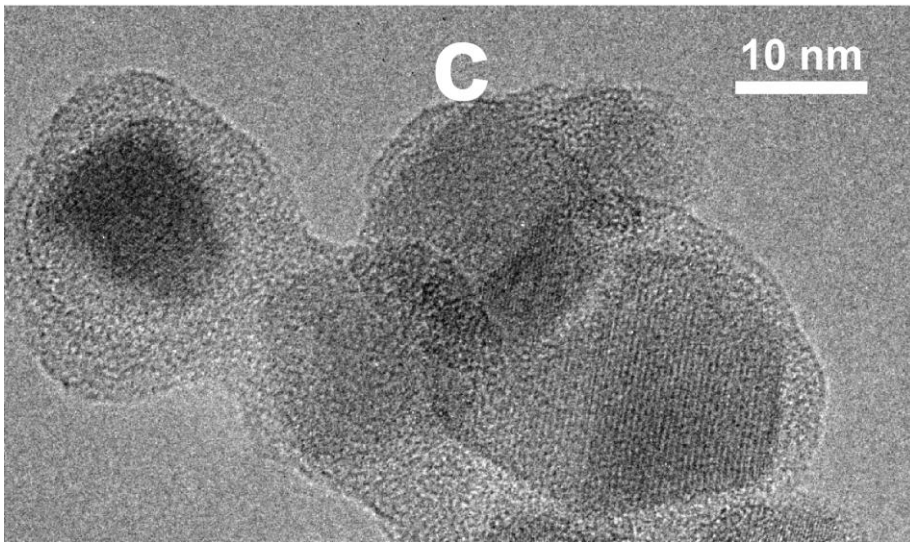
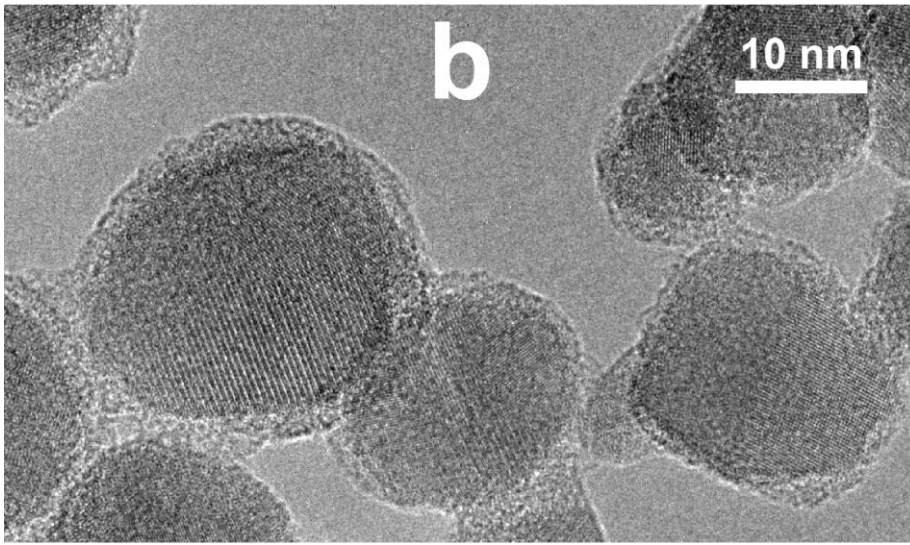
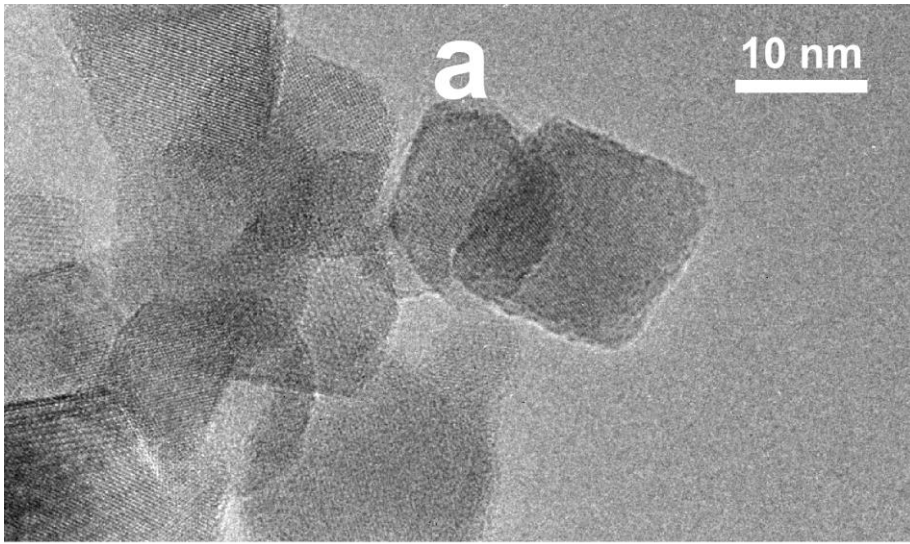
Figure 1



1

2

Figure 2



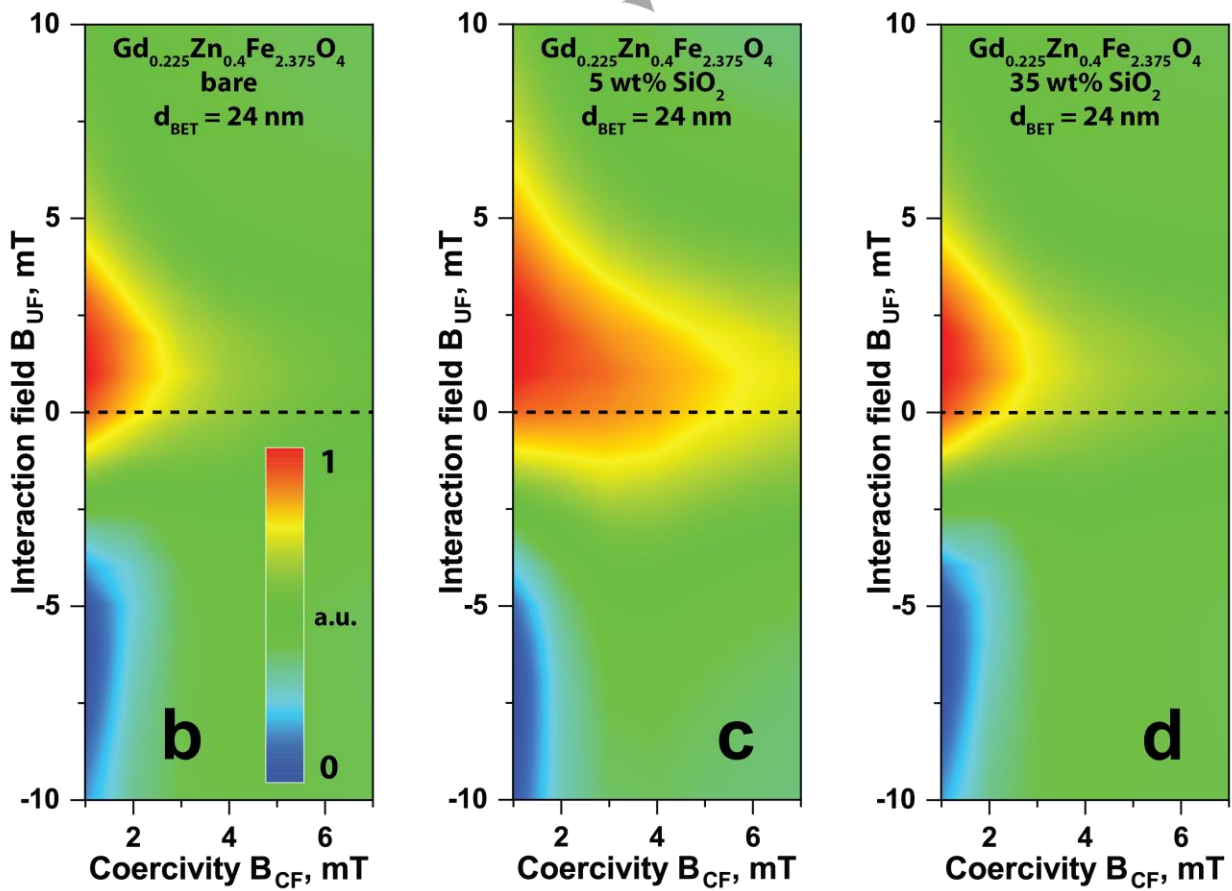
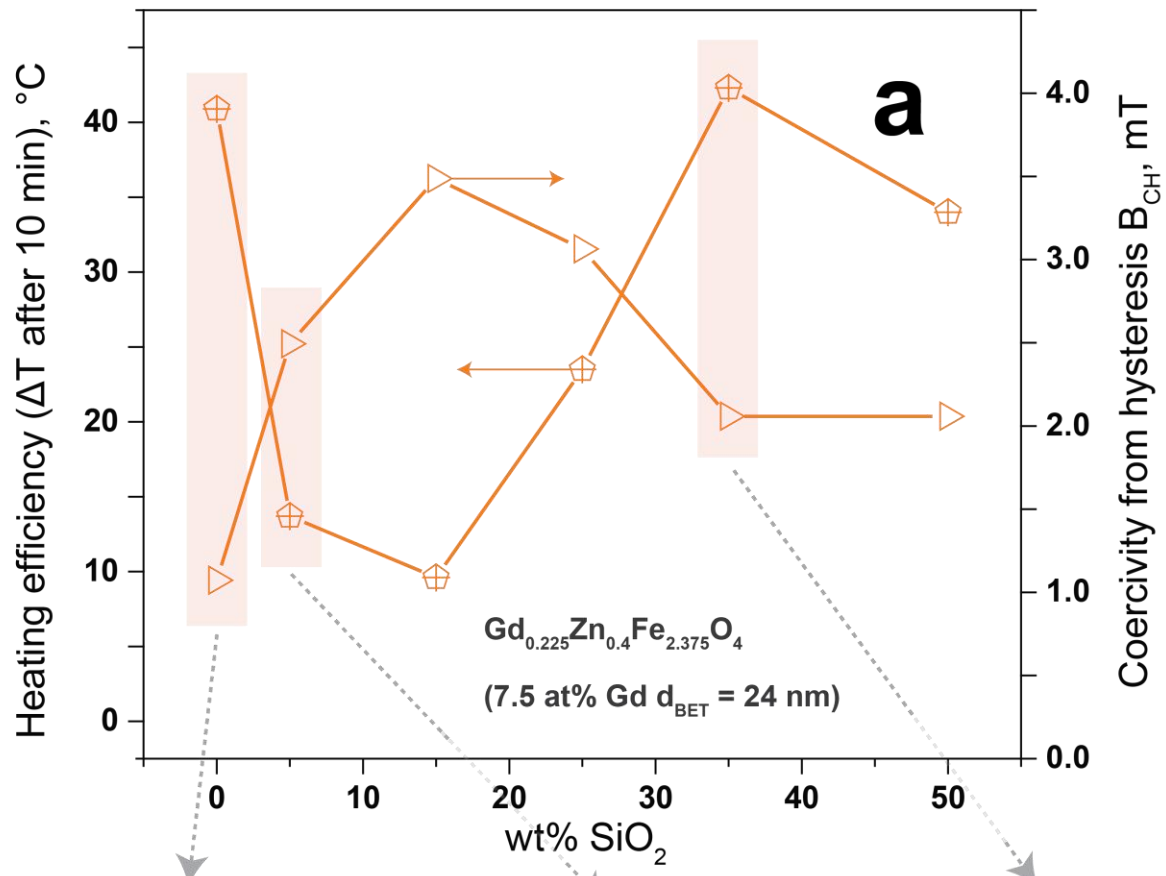
1

2

3

4

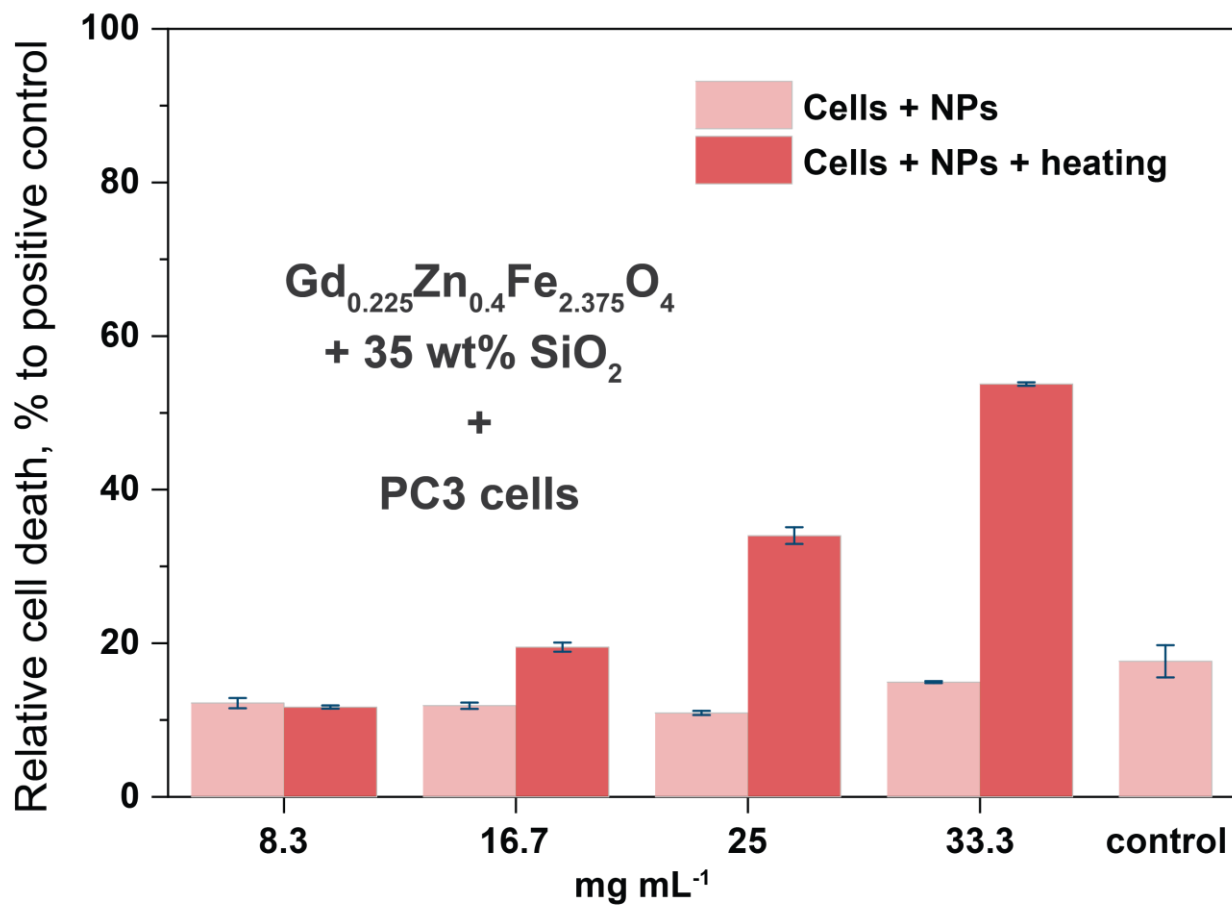
Figure 3



1

2

Figure 4



1
2
3
4
5
6
7
8
9
10
11
12

Figure 6

1
2
3
4
5
6
7
8
9
10
11
12
13
14
15
16
17
18
19
20
21
22
23
24
25
26
27
28

SUPPORTING INFORMATION

Coercivity determines magnetic particle heating

Fabian H.L. Starsich¹, Christian Eberhardt², Andreas Boss², Ann. M. Hirt³, Sotiris E. Pratsinis^{1,}*

¹Particle Technology Laboratory, Institute of Process Engineering, Department of Mechanical and Process Engineering, ETH Zurich, Sonneggstrasse 3, CH-8092 Zurich, Switzerland

²Institute of Diagnostic and Interventional Radiology, University Hospital Zürich, Rämistrasse 100, CH-8091 Zürich, Switzerland.

³Institute of Geophysics, ETH Zürich, Sonneggstrasse 5, CH-8092 Zürich, Switzerland.

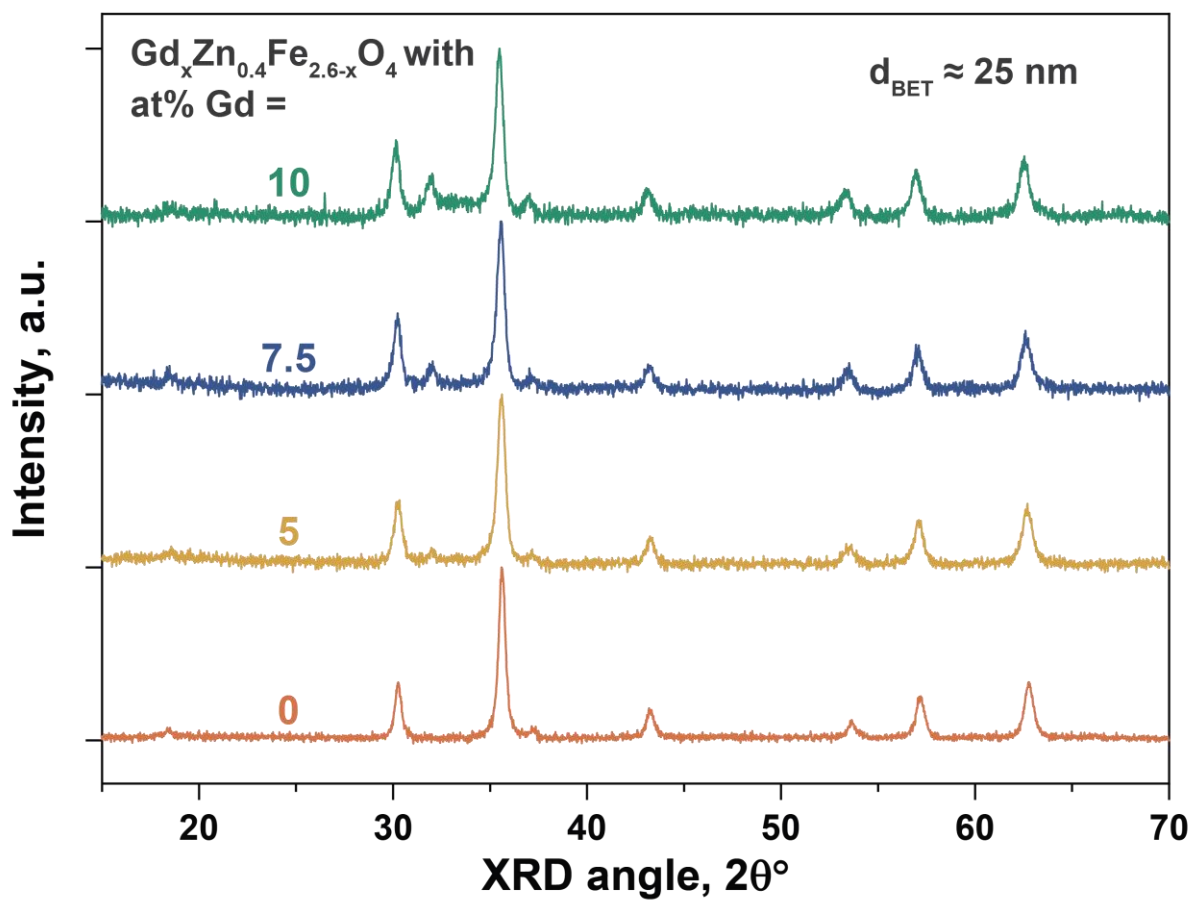
*Corresponding author:

Sotiris E. Pratsinis; Tel.: +41 44 632 31 80; fax: +41 44 632 15 95; e-mail: sotiris.pratsinis@ptl.mavt.ethz.ch

06.01.2021

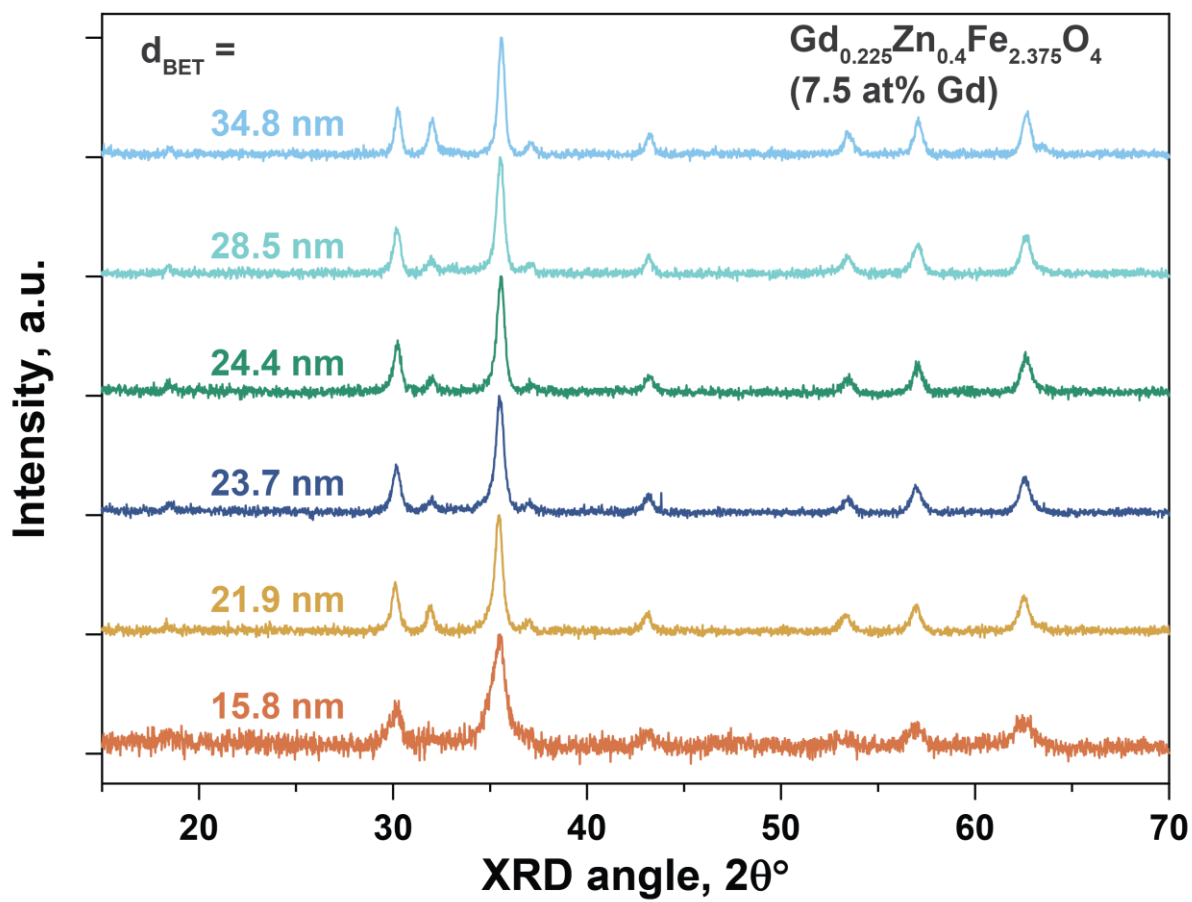
Submitted to:

Advanced Healthcare Materials

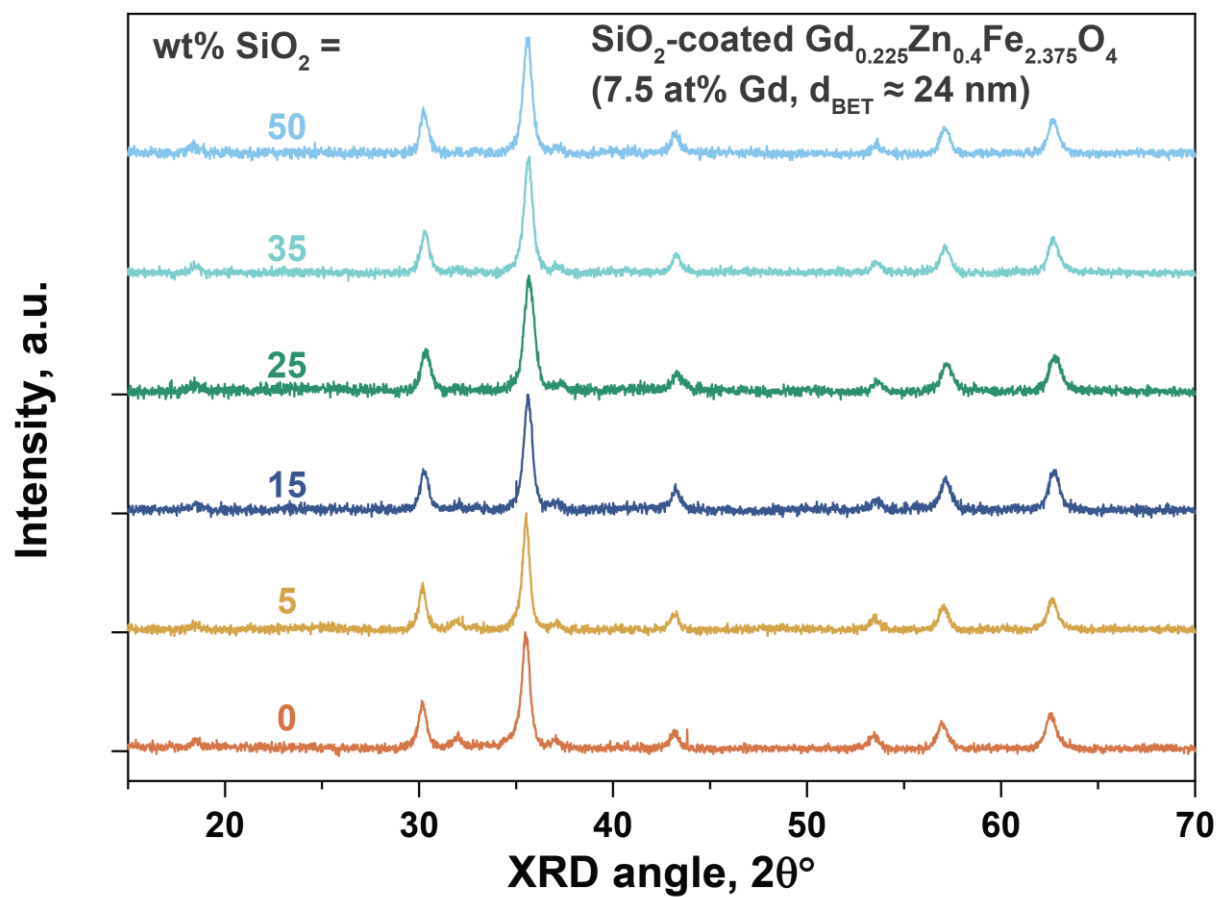


1
2 **Figure S1:** X-ray diffraction patterns of $\text{Gd}_x\text{Zn}_{0.4}\text{Fe}_{2.6-x}\text{O}_4$ with varying Gd content (0-30 at%) and
3 $d_{\text{BET}} = 25 \text{ nm}$.

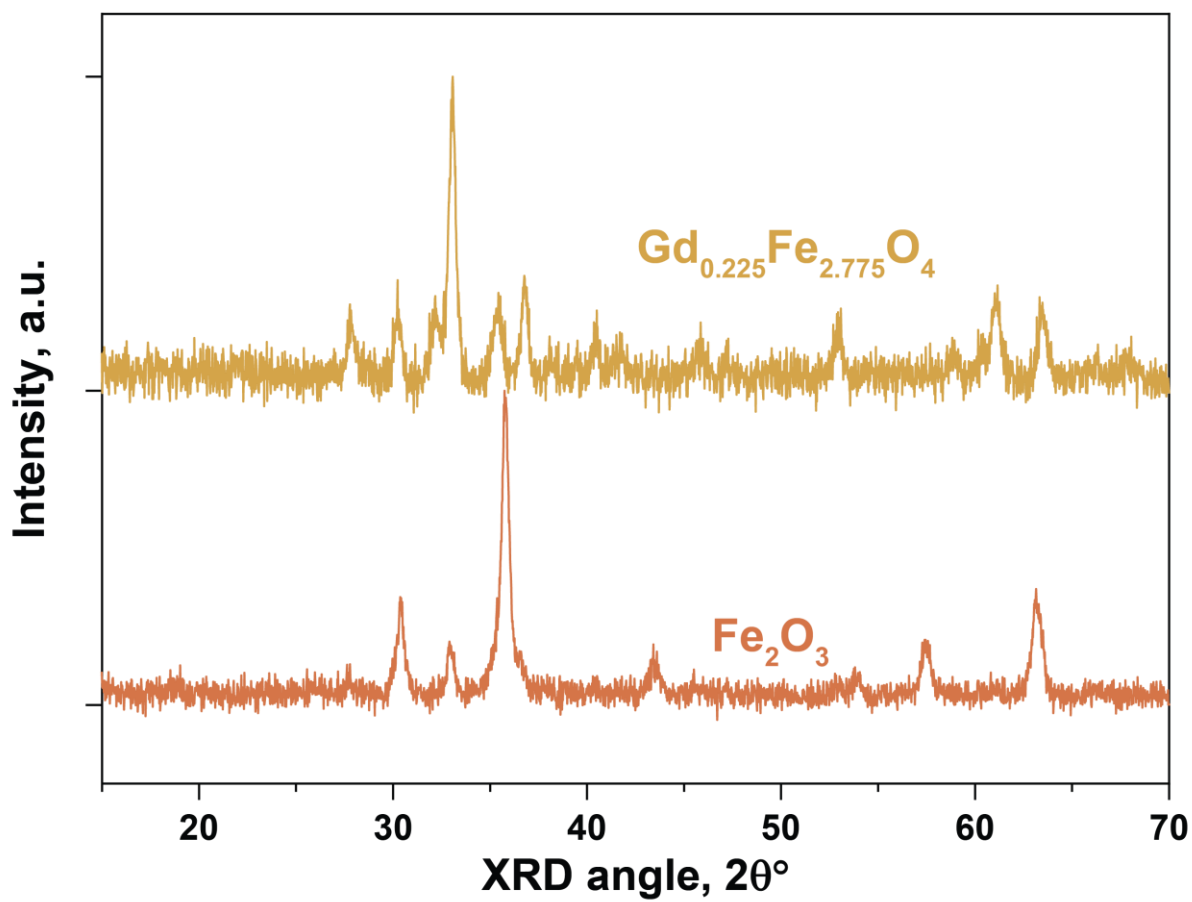
4



1
2 **Figure S2:** X-ray diffraction patterns of $\text{Gd}_{0.225}\text{Zn}_{0.4}\text{Fe}_{2.375}\text{O}_4$ (7.5 at% Gd) with varying d_{BET} .

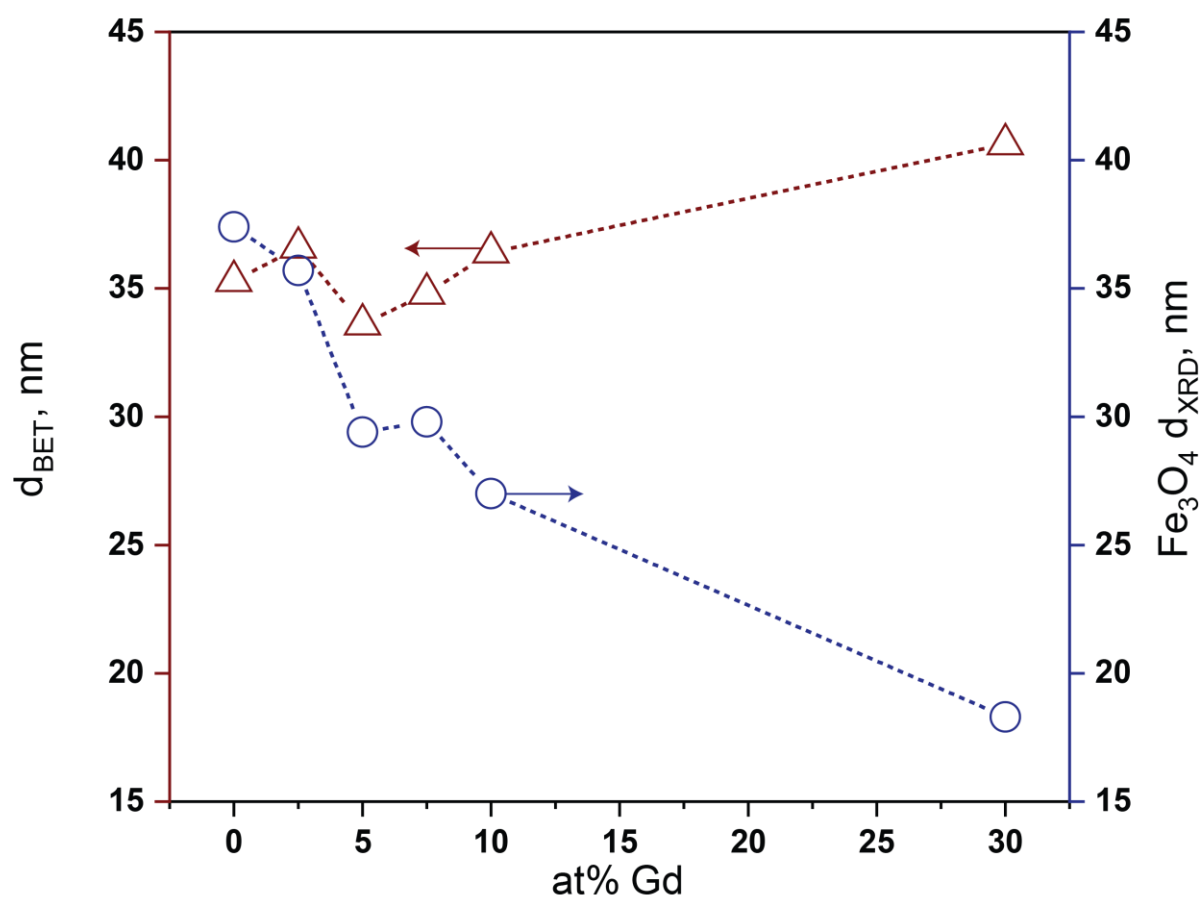


1
2 **Figure S3:** X-ray diffraction patterns of SiO_2 -coated $\text{Gd}_{0.225}\text{Zn}_{0.4}\text{Fe}_{2.375}\text{O}_4$ (7.5 at% Gd, $d_{\text{BET}} = 24$ nm) with
3 varying SiO_2 content (0-50 wt%).



1
2 **Figure S4:** X-ray diffraction patterns of $Gd_{0.225}Fe_{2.775}O_4$ and Fe_2O_3 .

3



1
 2 **Figure S5:** Primary particle (red triangles, left axis) and crystal (blue circles, right axis) as a function of
 3 at% Gd.

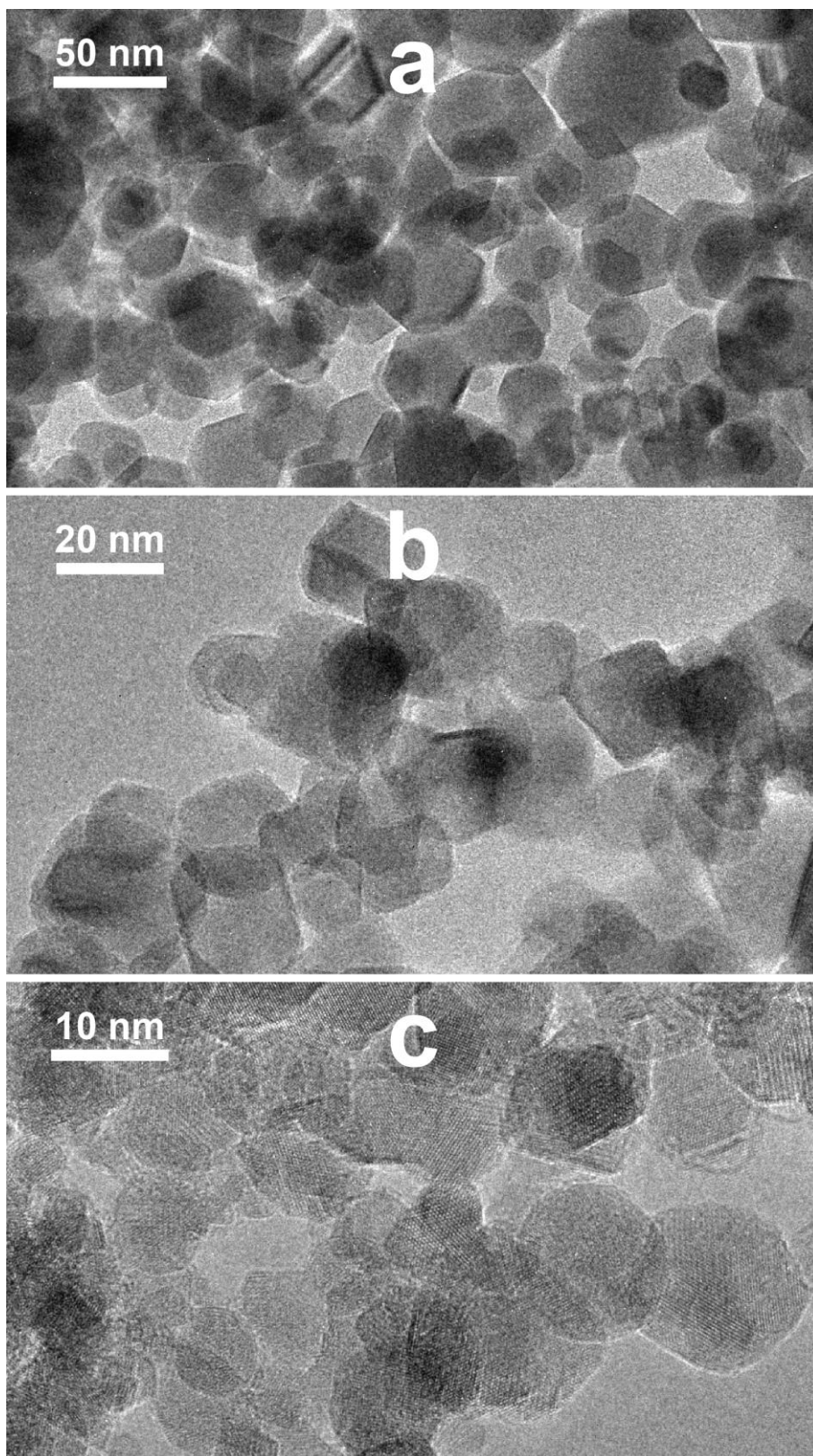
4

5

6

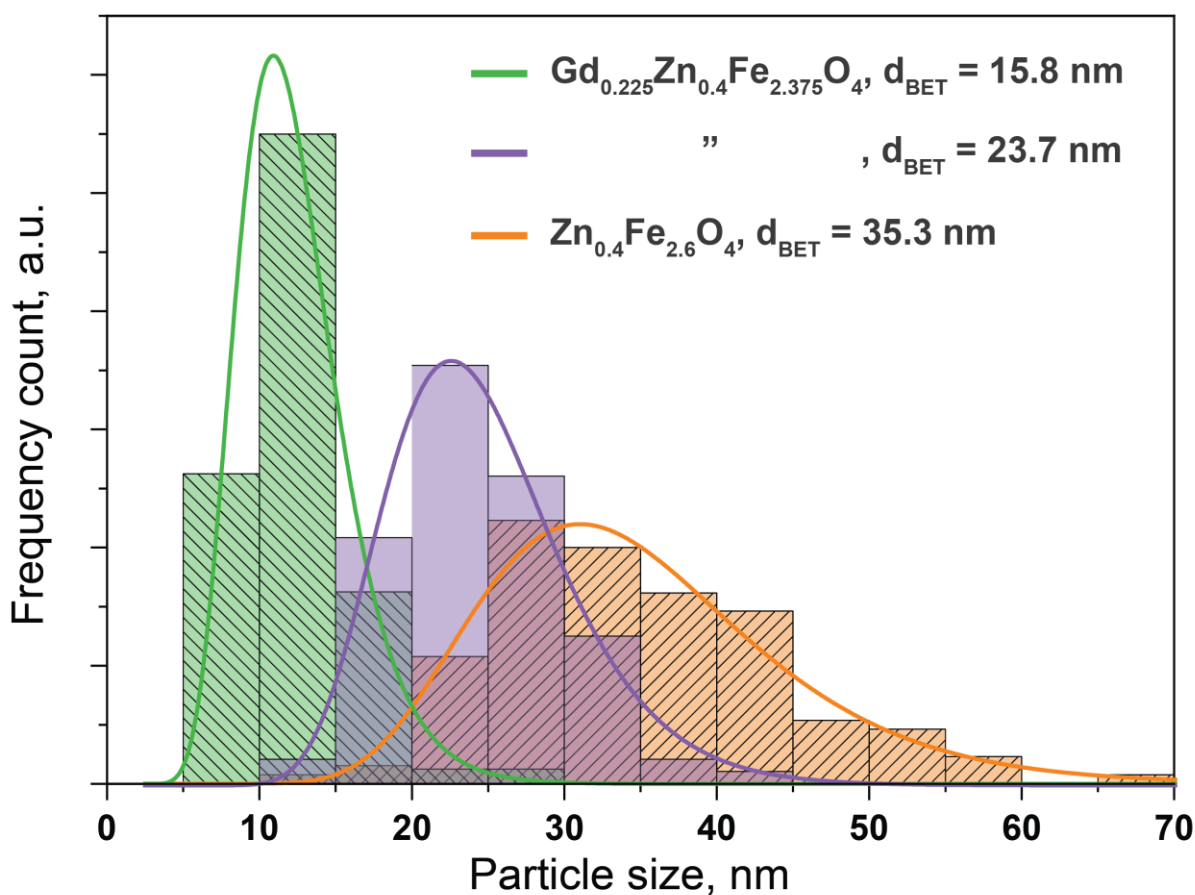
7

8



1

2 **Figure S6:** Transmission electron images of bare $\text{Gd}_{0.225}\text{Zn}_{0.4}\text{Fe}_{2.375}\text{O}_4$ nanoparticles with (a) $d_{\text{BET}} = 15.8$ nm
3 and (b) 23.7 nm, as well as of (c) bare $\text{Zn}_{0.4}\text{Fe}_{2.6}\text{O}_4$ nanoparticles with $d_{\text{BET}} = 35.3$ nm.

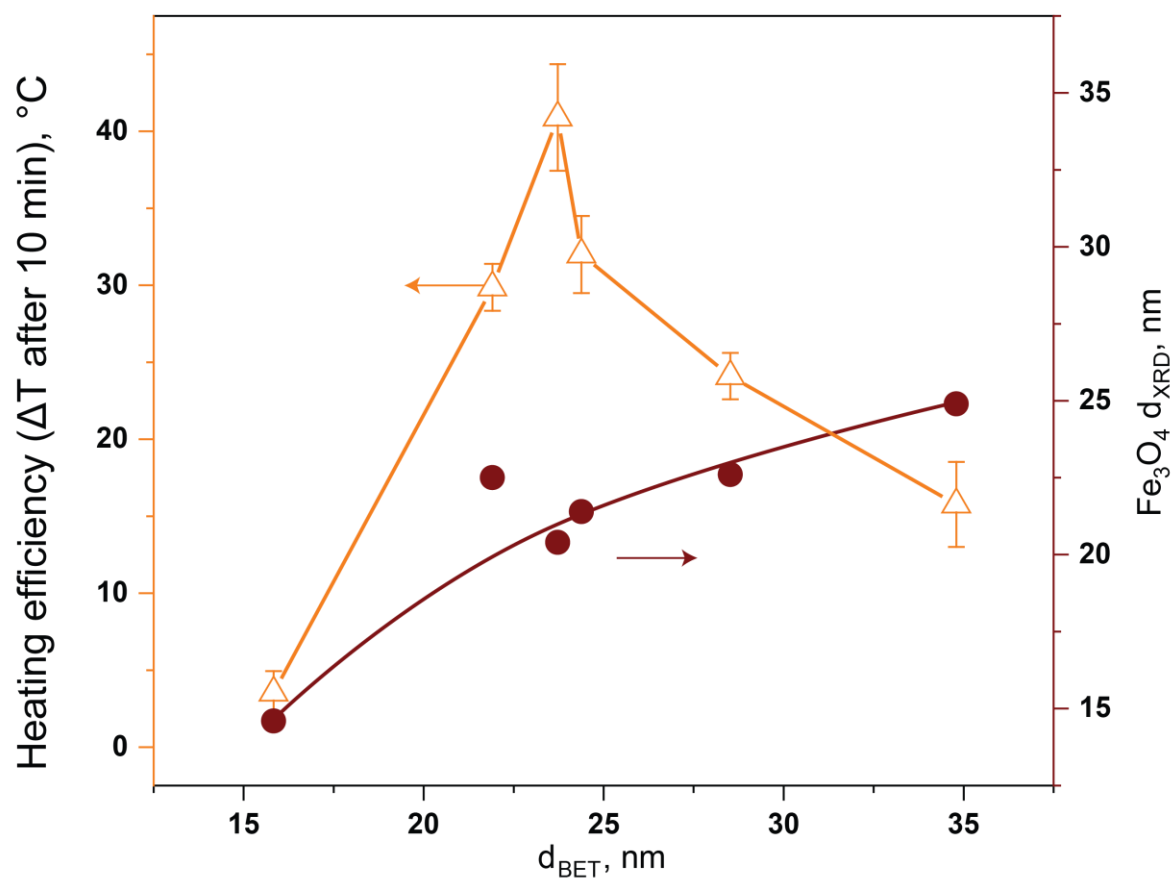


1

2 **Figure S7:** Primary particle size distribution of bare $\text{Gd}_{0.225}\text{Zn}_{0.4}\text{Fe}_{2.375}\text{O}_4$ nanoparticles with $d_{\text{BET}} = 15.8$ nm
 3 and 23.7 nm, as well as of bare $\text{Zn}_{0.4}\text{Fe}_{2.6}\text{O}_4$ nanoparticles with $d_{\text{BET}} = 35.3$ nm, as determined by image
 4 analysis of 80, 96 and 130 particles, respectively. Average primary particle size from TEM (green: 12.6 nm,
 5 violet: 24 nm, orange: 35.2 nm) correspond well to size from BET. Geometric standard deviations (green:
 6 1.32, violet: 1.24, orange: 1.33) indicate a narrow primary particle size-distribution.

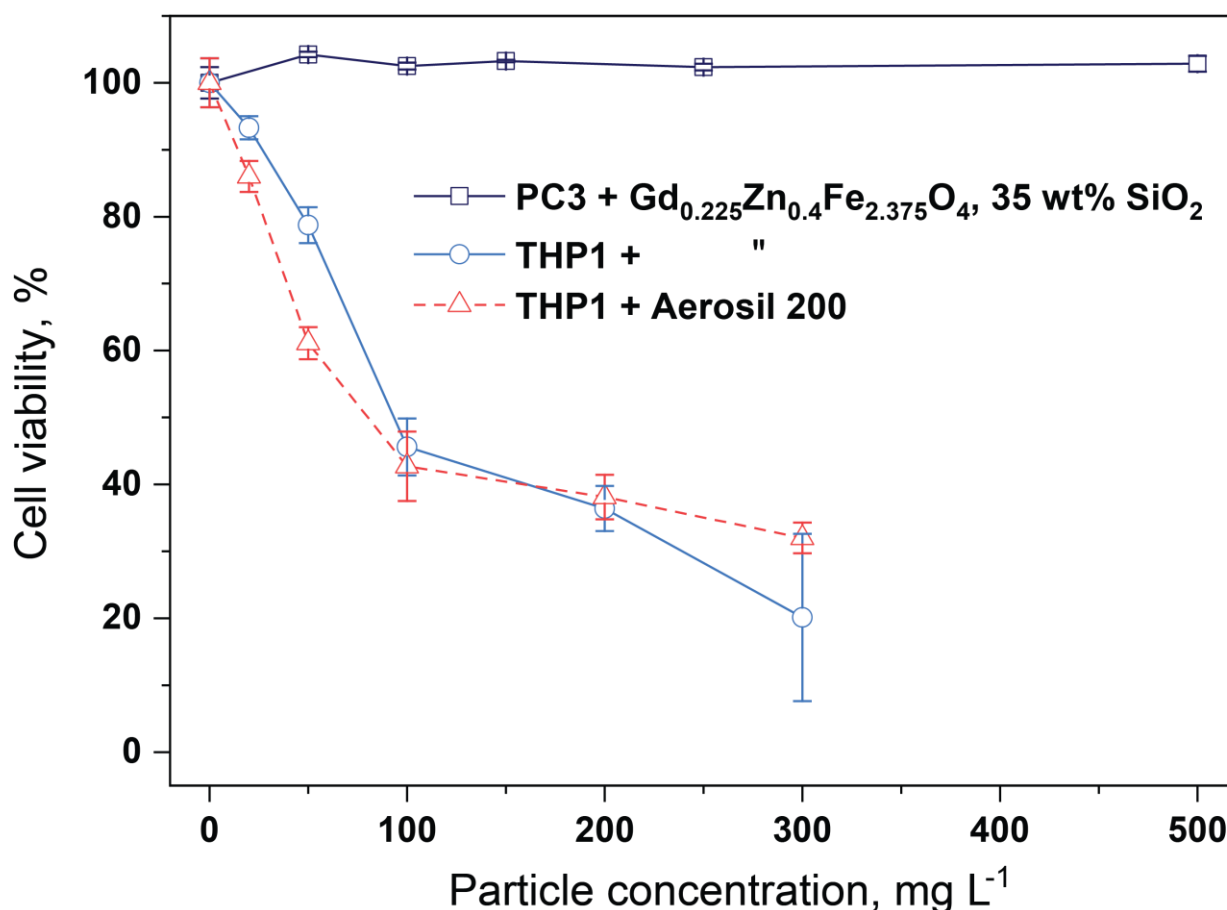
7

8



1
 2 **Figure S8:** Heating efficiency (triangles) and crystal size (circles) as a function of primary particle diameter,
 3 d_{BET} , obtained by N_2 adsorption.

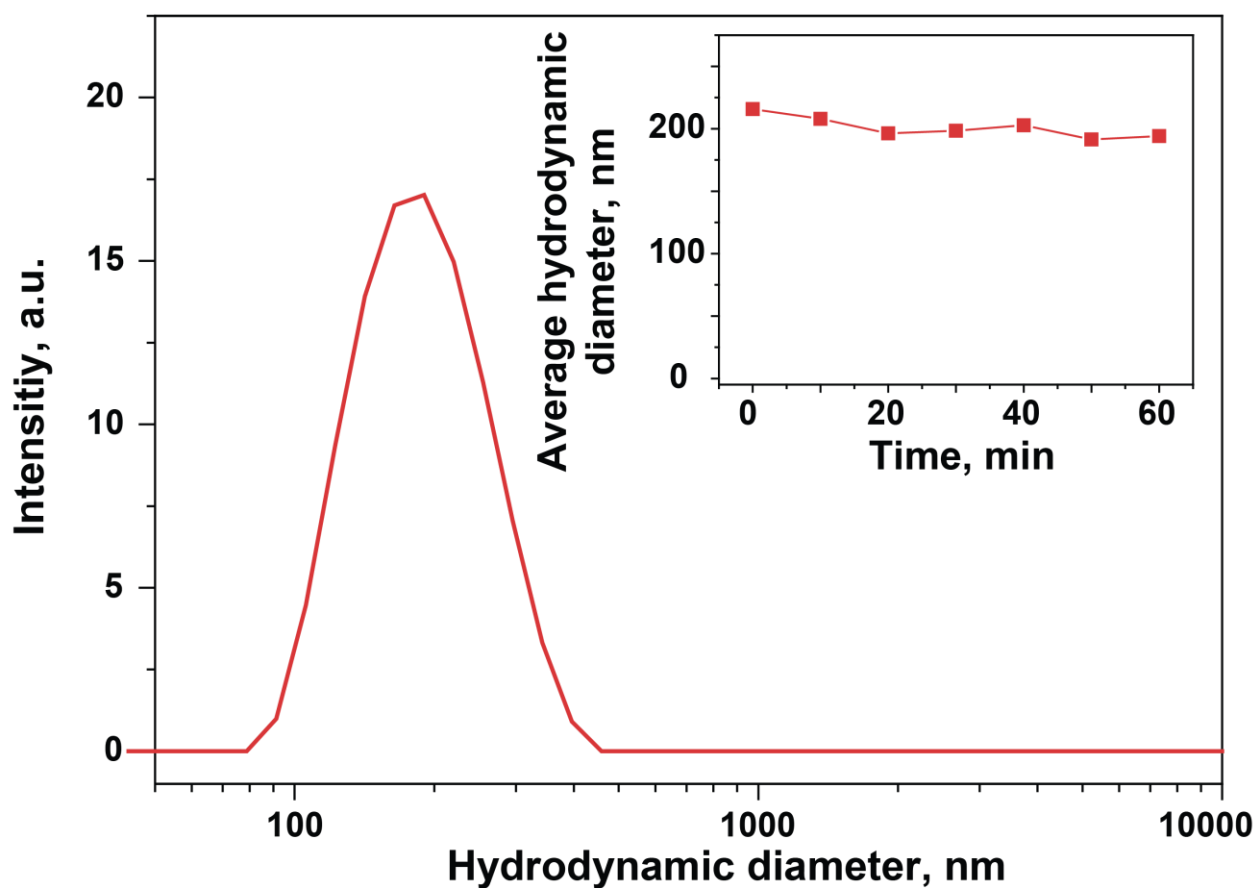
4



1
2 **Figure S9:** Viability of cancerous cells after incubation for 24 h with SiO₂ coated (35 wt%)
3 Gd_{0.225}Zn_{0.4}Fe_{2.375}O₄ (7.5 at% Gd) as well as commercial SiO₂ (Aerosil 200) nanoparticles at different
4 concentrations. The susceptible THP1 cells show minor toxicity up to 100 mg L⁻¹, very comparable for both
5 investigated nanoparticles. Higher nanoparticle concentrations cause only a small further decrease in
6 viability. Aerosil 200 is considered biocompatible and is frequently used in biological applications.^[60] The
7 fact that as-prepared SiO₂ coated Gd_{0.225}Zn_{0.4}Fe_{2.375}O₄ nanoparticles show comparable biocompatibility
8 suggests that the system can indeed be used for the selective destruction of diseased cells *in vivo*.
9 Interestingly using PC3 cells instead, the applied nanoparticles do not show any toxicity up to 500 mg L⁻¹.

10

11



1
 2 **Figure S10:** Hydrodynamic size distribution of PEGylated SiO₂-coated (35 wt%) Gd_{0.225}Zn_{0.4}Fe_{2.375}O₄
 3 (7.5 at% Gd) nanoparticles measured by dynamic light scattering. The suspension was prepared at a particle
 4 concentration of 0.1 mg mL⁻¹ of H₂O. Inset shows average hydrodynamic diameter over time.

1 **Table S1:** Summary of process parameters and material properties.

Synthesis Parameters				Composition			Particle Properties					
x	y	Tube	C _{metal}	Formula	Gd	SiO ₂	SSA	d _{BET}	d _{XRD}	ΔT after 10 min	M _s	B _{CH}
mL min ⁻¹	L min ⁻¹	cm	M		at%	wt%	m ² / g	nm	nm	°C	emu / g	mT
8	3	30	0.6	Zn _{0.4} Fe _{2.6} O ₄	0		32.89	35.3	35.1	0.83	73.42	9.48
8	3	30	0.6	Gd _{0.075} Zn _{0.4} Fe _{2.525} O ₄	2.5		31.08	36.6	33.3	3.37	67.42	8.48
8	3	30	0.6	Gd _{0.15} Zn _{0.4} Fe _{2.45} O ₄	5		33.22	33.6	25.5	6.97	53.06	5.99
8	3	30	0.6	Gd _{0.225} Zn _{0.4} Fe _{2.375} O ₄	7.5		31.52	34.8	26.1	15.77	38.38	3.99
8	3	30	0.6	Gd _{0.3} Zn _{0.4} Fe _{2.3} O ₄	10		29.62	36.4	23.4	19.1	25.72	1.99
8	3	30	0.6	Gd _{0.9} Zn _{0.4} Fe _{1.7} O ₄	30		23.91	40.6	18.3	-0.17	1.37	1.48
8	3	0	0.3	Gd _{0.225} Zn _{0.4} Fe _{2.375} O ₄	7.5		69.26	15.8	14.6	3.53	20.11	0.98
5	5	20	0.3	Gd _{0.225} Zn _{0.4} Fe _{2.375} O ₄	7.5		50.05	21.9	22.5	29.87	35.24	0.98
7	5	20	0.3	Gd _{0.225} Zn _{0.4} Fe _{2.375} O ₄	7.5		44.97	24.4	21.4	32	39.49	1.99
8	3	20	0.3	Gd _{0.225} Zn _{0.4} Fe _{2.375} O ₄	7.5		38.45	28.5	22.6	24.1	35.85	2.49
7	5	20	0.3	Fe ₂ O ₃	0		46.51	25	23	1.17	39.98	15.04
7	5	20	0.3	Zn _{0.4} Fe _{2.6} O ₄	0		45.8	25.3	25.7	9.47	68.38	5.99
7	5	20	0.3	Gd _{0.225} Fe _{2.775} O ₄	7.5		40.59	27	25.2	-0.67	3.88	6.49
7	5	20	0.3	Gd _{0.15} Zn _{0.4} Fe _{2.45} O ₄	5		44.5	25.1	20.3	22.87	49.27	2.98
7	5	20	0.3	Gd _{0.3} Zn _{0.4} Fe _{2.3} O ₄	10		38.83	27.8	21.1	25.97	28.09	0.98
7	5	20/30	0.3	Gd _{0.225} Zn _{0.4} Fe _{2.375} O ₄	7.5	0	46.23	23.7	20.4	40.9	37.3	0.98
7	5	20/30	0.3	Gd _{0.225} Zn _{0.4} Fe _{2.375} O ₄	7.5	5	44.63		23.8	13.7	45.99	2.49
7	5	20/30	0.3	Gd _{0.225} Zn _{0.4} Fe _{2.375} O ₄	7.5	15	54.74		18.3	9.6	51.51	3.49
7	5	20/30	0.3	Gd _{0.225} Zn _{0.4} Fe _{2.375} O ₄	7.5	25	54.09		14.3	23.5	50.64	2.98
7	5	20/30	0.3	Gd_{0.225}Zn_{0.4}Fe_{2.375}O₄	7.5	35	69.84		18.3	42.3	53.55	2.06
7	5	20/30	0.3	Gd _{0.225} Zn _{0.4} Fe _{2.375} O ₄	7.5	50	97.21		17.5	34	44.85	2.06

